ISSN 1063-7834, Physics of the Solid State, 2021, Vol. 63, No. 2, pp. 332–354. © Pleiades Publishing, Ltd., 2021.

LATTICE DYNAMICS

The Influence of Thermal Treatment on the Formation Mechanism of the Cu, Fe-Containing Nanocomposite Material Synthesized by the Sol–Gel Method

V. N. Nikolić[a, *], M. M. Vasić[b], J. Milikić[b], and J. F. M. L. Mariano[c, d]

[a] *Department of Theoretical and Condensed Matter Physics, "VINČA" Institute of Nuclear Sciences—National Institute of the Republic of Serbia, University of Belgrade, Belgrade, Serbia*

[b] *Faculty of Physical Chemistry, University of Belgrade, Belgrade, Serbia*

[c] *Universidade do Algarve, FCT, Campus de Gambelas, 8005-139 Faro, Portugal*

[d] *Center of Physics and Engineering of Advanced Materials (CeFEMA), IST, Universidade de Lisboa, 1096-001 Lisboa, Portugal*

** e-mail: violeta@vin.bg.ac.rs*

Received September 22, 2020; revised October 2, 2020; accepted October 6, 2020

Abstract—The nanocomposite samples, containing copper and iron species in the silica matrix, were prepared by annealing at temperatures up to 1100°C. The samples were investigated by X-ray diffraction analysis, Fourier transform infrared spectroscopy, and cyclic voltammetry. The results of the performed study depict to the presence of a temperature gradient, which acts on the sample during the annealing treatment in the furnace. For the first time, the influence of the temperature gradient on the formation mechanism of the samples was discussed.

Keywords: temperature gradient, nanocomposite, sol–gel, XRD, FTIR

DOI: 10.1134/S1063783421020207

1. INTRODUCTION

Sol–gel synthesis method enables obtaining multiphase nanocomposite samples that contain different phases in the pores of the silica matrix [1]. The growth and size of the phases present in silica pores are limited by the size of the pores. The formation of the nanoparticles in the silica pores is based on the co-precipitation of the synthesis products (obtained by using the metal precursors) in the silica pores [2]. The product of the co-precipitation synthesis is characterized by a wide particle-size distribution in the silica pores.

The characterization technique, most commonly used to gain deeper insight into the particles size and shape distribution (transmission electron microscopy, TEM), is not suitable for investigating the multiphase, nanocomposite samples containing multiphase nanoparticles in the pores of silica matrix, prepared by auto- or acid-sol–gel syntheses [2], due to the overlap of the very small nanoparticles of different phases present in the pores of the silica matrix.

On the other hand, a deeper insight into the particle size and shape of the sample does not provide information about the geometrical distribution of the phases and their distance from the surface of the annealed samples, because the TEM technique measures the 2D projection of a 3D sample; i.e., the TEM measurements do not enable insight in the change in phase composition within silica pores with the pore depth. Nevertheless, a better understanding of the geometric distribution of the phases in the mentioned samples is important for a deeper insight into the sequence of phase transformations, which is an important part of the formation mechanism of the prepared samples.

The factor, not usually considered in articles investigating the characterization of samples prepared by the sol–gel method, is the temperature gradient T_{grad}, to which the sample is exposed in the furnace. The scientific studies based on the characterization of the samples prepared by the sol–gel method usually do not comment type of the furnace used for the thermal treatment of the samples [3–65], i.e., do not specify the geometrical distribution of the heaters in the furnace. The geometrical distribution of the heaters in the furnace is important because it determines the temperature gradient T_{grad} within the furnace. This also could be one of the reasons why different researchers get different results for practically the same synthesis procedures performed in different laboratories.

Most of the different types of furnaces, used in the research laboratories, have the geometrical distribu-

tion of the heaters that allows the sample to be irradiated uniformly with the heat. Since the annealed samples are characterized by a certain thickness (i.e., the investigated samples are 3D macroscopic objects, consisted of nm-sized particles), they experienced the impact of T_{grad}. Due to the presence of a T_{grad}, in the first moment when the desired temperature in the furnace is reached, the surface parts of the samples are first exposed to the annealing temperature, which initiates a pronounced increase of surface particles sizes and accelerates their phase transformations. Further, due to the thickness of the sample and T_{grad}, the same temperature, to which the sample surface is exposed, is achieved later (Δt) in the deeper volume of the sample, which means that a phase transformation occurring on the surface still does not appear in the deeper sample volume (in the first moment when the annealing temperature is achieved). Nevertheless, because the thickness of the sample is very small, no matter how short is the time Δt from a macroscopic point of view, and despite the fact that the sample is kept at annealing temperature T_{ann} for a certain annealing time t_{ann}, at the nanometer level, the T_{grad} significantly affects the sequence of phase transformations, occurring in the sample. The results obtained in the presented research indirectly prove that T_{grad} determines the sequence of phase transformations in the sample.

In this study, we investigated the nanocomposite samples, consisted of different number of phases (dependent on the applied annealing temperature), such as: monoclinic and orthorhombic copper hydroxide nitrate $Cu_2(OH_3)NO_3$, copper oxide CuO, spinel phases (magnetite Fe_3O_4/maghemite γ-Fe_2O_3, or cubic copper ferrite c-$CuFe_2O_4$), hematite α-Fe_2O_3, tetragonal copper ferrite t-$CuFe_2O_4$, and different types of silica SiO_2, amorphous and crystalline (cristobalite, quartz, and tridymite). Samples were prepared by the sol–gel method, in order to gain a deeper insight into the phase transformations and the mechanism of formation of the investigated samples. The samples are characterized by X-ray diffraction (XRD), Fourier transform infra-red spectroscopy (FTIR), and cyclic voltammetry measurements (CV).

2. EXPERIMENTAL

The native sample to be subjected to thermal treatment at various temperatures was synthesized by the sol–gel method, starting from the iron and copper cation salts [43, 66–68]. The self-catalyzed sol–gel synthesis implied the next procedure: two catalyst solutions, containing Fe^{3+} and Cu^{2+}, were prepared in separated beakers by the dissolution of salts in 10 mL of water cations ($Fe(NO_3)_3 \cdot 9H_2O$ and $Cu(NO_3)_2 \cdot 3H_2O$ were mixed at the molar ratio 0.01 : 0.01). Then, the solution of Cu^{2+} cations was transferred into the beaker with Fe^{3+} cations. The solution was magnetically stirred until it became a homogeneous green solution. In the separated beaker, an alkoxide solution was prepared (TEOS, H_2O, and C_2H_5OH at the molar ratio 0.001 : 0.06 : 0.06). The alcohol solution was added to the stirring solution and stirred at room temperature for 4 h and 30 min. After the gelation procedure, the alcohol was dried at 90°C for 24 h. Dried alcogel was characterized by the brown color and the presence of azure-blue powder, on the surface of the sample, surrounded with white powder.

The dried alcogel was left in the open air for 24 h, and it was observed that the amount of blue powder increased in the entire volume of the sample. Thereafter, parts of the dried alcogel, taken from the same batch, were annealed in the air atmosphere at various temperatures: 200, 400, 600, 700, 800, 900, 1000, 1050, and 1100°C, for 3 h. Dried alcogel was labeled with the letter S, while the annealed samples were labeled with the same mark (letter and number), indicating annealing temperature, to which the sample was exposed (S200, S400, S600, S700, S800, S900, S1000, S1050, and S1100). The samples were annealed in a furnace, manufactured by Vims Elektrik d.o.o., Tršić, Serbia.

XRD measurements were performed by a Rigaku RINT-TTRIII diffractometer with Ni-filtered CuK_α monochromatic radiation ($\lambda = 1.5418$ Å). The diffraction patterns were collected at room temperature over a 2θ range: 15°–80°, by a step of 0.02°, and a speed duration time 0.5 min. The Inorganic Crystals Structure Database [69] was used to analyze the recorded patterns. The analysis of the patterns was done by using the Rietveld method, employing the MAUD software [70].

FTIR measurements were done by a Nicolet IS 50 FTIR spectrometer, in the mid-IR spectral region of 4000–400 cm^{-1}, using a resolution of 4 cm^{-1} and 64 co-added scans. Sampling technique applied to measure spectra was attenuated total reflectance (ATR).

Electrochemical characterization for the chosen samples (S, S800, and S1100) was done using Ivium V01107 potentiostat, in a three-electrode system with saturated calomel (SCE) as a reference, graphite rod as a counter, and S, S800, and S1100 as the working electrode. 1 M of potassium hydroxide KOH as supporting electrolyte was used. The current density of all electrodes was calculated with a geometric surface area (0.945 cm^{-2}), and potential was given relative to the potential of the SCE electrode. Cyclic voltammetry (CV) characterization of the S, S800, and S1100 electrodes was run in potential range from –1.1 to 0.5 V, at a scan rate of 25 mV s^{-1}, in 1 M of KOH (N_2-saturated). Preparation of the working electrodes (catalytic inks) was done by mixing 5 mg of the powder of the samples (S, S800, and S1100) and Vulcan carbon black (0.6 mg). The mixture was dispersed in 15 μL of polyvinylidene fluoride (PVDF) solution (2 wt % PVDF in N-methyl-2-pyrrolidone) and homogenized

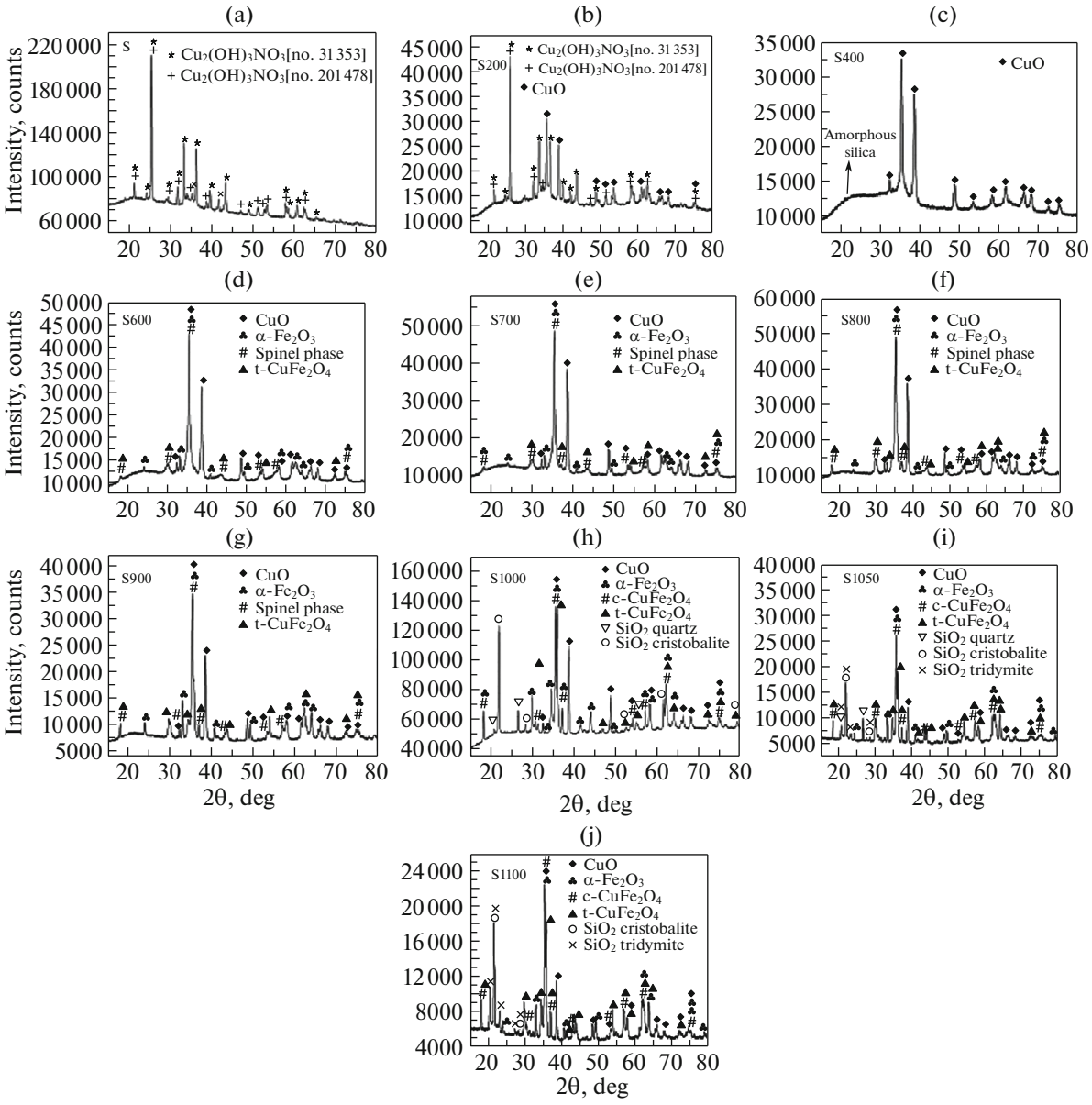

Fig. 1. Diffraction patterns of the (a) S; (b) S200; (c) S400; (d) S600; (e) S700; (f) S800; (g) S900; (h) S1000; (i) S1050; (j) S1100.

in an ultrasonic bath for 30 min. The working electrodes were made by depositing catalytic ink (10 μL) onto glassy carbon substrates and then drying at 110°C overnight.

3. RESULTS

3.1. XRD Measurements

Diffraction patterns of the investigated samples (S, S200, S400, S600, S700, S800, S900, S1000, S1050, and S1100) are presented in Figs. 1a–1j.

The symbols in the diffraction patterns indicate the phase present within the sample.

Phase transformations within the annealed samples, including the growth of nanoparticles, are induced by thermal treatment. The samples consisted of different phases listed below. According to XRD analysis, the sample S contains the crystalline copper salts $Cu_2(OH_3)NO_3$, monoclinic (ICSD card number: (no. 31353)) and orthorhombic phase (ICSD card number: (no. 201478)). If we recall the precursors used in the performed synthesis of the samples, as well the color of the investigated sample S, we can conclude about the phases presented in Fig. 1. The predominantly observed brown co-precipitate is impure, amorphous, copper silicate that consists of different phases containing cations of Cu, Fe, and Si (Fe_2O_3,

SiO_2, CuO, etc.) [71]. Azure-blue powder is $Cu_2(OH_3)NO_3$ phase, and white powder could be ascribed to silica. The small size of the nuclei of the presented phases prevents the detection of these phases by using XRD measurements, and only $Cu_2(OH_3)NO_3$ phase is observed in the diffraction pattern of the sample S. Further heat treatment reveals the appearance of different phases in the examined samples. Figure 1b shows that the sample S200 consists of dymorphs of copper salts $Cu_2(OH_3)NO_3$ and CuO (ICSD card: (no. 67850)). After annealing at 200°C, amorphous silica also can be detected by XRD measurements (Fig. 1b). Diffraction pattern of the sample S400 revealed disappearance of the $Cu_2(OH_3)NO_3$, and XRD analysis enabled detection of the only one crystalline phase, CuO (Fig. 1c).

It should be noted here that although the literature has revealed the difficulty to predict the exact mechanism of copper ferrite nanoparticles formation due to the presence of different intermediate species, such as $[Cu(H_2O)_6]^{2+}$, $Cu_2(OH)_3NO_3$, and $Cu(OH)_2$ [72, 73], the phase composition of samples S and S200 indicates that the compound $Cu_2(OH_3)NO_3$ has a more prominent role in the formation of copper ferrite nanoparticles.

Annealing at higher temperatures (Figs. 1d–1j) revealed the presence of new phases: copper ferrite phases (both structures, tetragonal $CuFe_2O_4$ (no. 16666) and cubic $CuFe_2O_4$ (no. 153013)), iron oxide phases (magnetite Fe_3O_4 (no. 165105)/maghemite γ-Fe_2O_3 (no. 172905)) and hematite α-Fe_2O_3 (no. 182839)), and silica (SiO_2) polymorphs (cristobalite (no. 30269), quartz (no. 16331), and tridymite (no. 94090)). The phase transformations are governed by thermal treatment. The positions of the diffraction maxima, on the basis of which the coherent scattering domain size of the investigated phases was determined, are 25.8° for monoclinic $Cu_2(OH_3)NO_3$, 34.1° for orthorhombic $Cu_2(OH_3)NO_3$, 32.5° for CuO, 30.2° for spinel phase, 29.9° for t-$CuFe_2O_4$, 33.2° for α-Fe_2O_3, 21.9° for cristobalite, 20.8° for quartz, and 21.7° for tridymite. The deconvolution of the diffraction maxima was performed in the cases when it was not possible to deduce the exact value based on the recorded diffraction maximum. For better insight into the phase transformations induced by thermal treatment, the results of XRD analysis are shown in Table 1.

In Table 1, the increase in the amount of the discussed phase indicates a pronounced formation of the mentioned phase. In contrast, a decrease in the amount of a phase indicates the consumption of the investigated phase, amount of which decreases in the process of formation of a new phase. The behavior of the presented phases, governed by the thermal treatment, will be discussed below.

The first glance at Table 1 reveals that the spinel phase was present with the smallest amount in the investigated samples. The dominant phase in samples annealed at temperatures below 400°C is the copper salt; in the temperature interval from 400 to 1000°C, the most represented phase is CuO up to 1000°C, when the amount of formed t-$CuFe_2O_4$ begins to exceed the amount of CuO phase. Consequently, t-$CuFe_2O_4$ represents the most abundant phase at temperatures ≥1000°C.

It is interesting to note that the crystallite size of $Cu_2(OH)_3NO_3$ structures remains unchanged during heat treatment, although the two structures of this compound are presented in significantly different amounts. Since the amount of monoclinic $Cu_2(OH)_3NO_3$ decreases by 17% after annealing at 200°C, and the amount of orthorhombic $Cu_2(OH_3)NO_3$ decreases by 5% (Table 1), it is obvious that the CuO phase, which is observed at 200°C (22%), originates from both different structures of $Cu_2(OH)_3NO_3$ (monoclinic and orthorhombic), which confirms the presence of different structurally ordered CuO phases in the examined samples and their influence on $CuFe_2O_4$ structural transformation [44]. Recall, at 400°C, the phase transformation of $Cu_2(OH)_3NO_3$ into CuO is complete, and the only observed crystalline phase is CuO.

Two remarks important for understanding the structural and phase transformations of the examined samples will be commented below. First, the diffraction pattern of the samples S200 and S400 did not enable distinguishing between potentially presented, different CuO structures (described by the space group C2/c and less symmetric space group Cc) [44], which is of importance for determination of the structure of $CuFe_2O_4$ phase that is being formed under the further thermal treatment at higher temperatures. The next important fact is that the nuclei of the iron and copper oxide phases are formed at the same temperature (Fig. 1) [43]. Despite this, smaller amount of iron precursors resulted in masking the presence of crystalline iron oxide phases by the predominant copper cation [43], so the crystalline iron oxide phases cannot be observed after annealing at lower temperatures. Accordingly, the first observation of iron species occurs at 600°C.

The behavior of the spinel phase is the most difficult to interpret because it is represented by the lowest amount in the samples. Recall that one of the precursors used in the synthesis was iron salt, which is often used in a typical synthesis involving the preparation of copper ferrite. The part of the mechanism of formation of copper ferrite nanoparticles, synthesized from precursors of copper salts and iron nitrate (see Section 2), involves the formation of various ferric ferrous hydroxy complexes $[(Fe(OH)_n(H_2O)(6-n)(3-n)^+_{aq}]$ [74–76]) that are converted into 2L-Fhyd by heat treatment; further thermal treatment induces

Table 1. Phase composition and average coherent scattering domain size of individual crystalline phases in the prepared samples

Sample	Observed phases	Phase composition, wt %	Coherent scattering domain size, nm
S	$Cu_2(OH_3)NO_3$ [no. 31353]	79 ± 2	60 ± 4
	$Cu_2(OH_3)NO_3$ [no. 201478]	21 ± 2	31 ± 2
S200	$Cu_2(OH_3)NO_3$ [no. 31353]	62 ± 3	61 ± 4
	$Cu_2(OH_3)NO_3$ [no. 201478]	16 ± 3	30 ± 3
	CuO	22 ± 3	*1
S400	CuO	100	32 ± 2
S600	CuO	64 ± 3	39 ± 3
	t-$CuFe_2O_4$	18 ± 2	16 ± 2
	α-Fe_2O_3	16 ± 2	37 ± 3
	Spinel phase	2 ± 1	18 ± 2
S700	CuO	65 ± 3	48 ± 3
	t-$CuFe_2O_4$	21 ± 3	19 ± 2
	α-Fe_2O_3	12 ± 3	42 ± 4
	Spinel phase	2 ± 1	21 ± 2
S800	CuO	60 ± 3	50 ± 3
	t-$CuFe_2O_4$	26 ± 3	24 ± 2
	α-Fe_2O_3	10 ± 2	40 ± 4
	Spinel phase	4 ± 1	20 ± 2
S900	CuO	45 ± 3	54 ± 3
	t-$CuFe_2O_4$	32 ± 2	30 ± 3
	α-Fe_2O_3	20 ± 2	45 ± 4
	Spinel phase	3 ± 1	33 ± 3
S1000	CuO	24 ± 2	54 ± 4
	t-$CuFe_2O_4$	44 ± 2	41 ± 3
	α-Fe_2O_3	*2	40 ± 5
	Spinel phase	2 ± 0.5	32 ± 3
	Quartz SiO_2	7 ± 2	48 ± 4
	Cristobalite SiO_2	22 ± 3	38 ± 3
S1050	CuO	21 ± 2	53 ± 4
	t-$CuFe_2O_4$	33 ± 3	40 ± 3
	α-Fe_2O_3	18 ± 3	41 ± 4
	Spinel phase	3 ± 1	31 ± 3
	Quartz SiO_2	3 ± 1	80 ± 7
	Cristobalite SiO_2	15 ± 1	41 ± 3
	Tridymite SiO_2	7 ± 1	44 ± 4
S1100	CuO	21 ± 2	54 ± 4
	t-$CuFe_2O_4$	34 ± 3	40 ± 3
	α-Fe_2O_3	16 ± 2	40 ± 4
	Spinel phase	4 ± 1	33 ± 3
	Cristobalite SiO_2	15 ± 2	41 ± 3
	Tridymite SiO_2	10 ± 2	48 ± 4

*1—It cannot be determined due to the significant overlapping of the XRD peaks of the CuO phase with the peaks of other phases present in the sample. *2—The diffraction maximum used to determine the amount of α-Fe_2O_3 at this temperature was poorly visible, and it was not possible to reliably determine wt %.

their conversion into oxides [43]. Accordingly, given the mechanism of copper ferrite formation, the presence of spinel iron oxide phases (Fe_3O_4 or γ-Fe_2O_3) can be assumed [43, 44]. Since spinel phase is obtained in an air atmosphere (see Experimental), taking into account the literature which confirms that passivation of magnetite nanoparticles by the surface layer of oxidized maghemite always occurs in air [77, 78], it can be postulated that both spinel iron oxide phases (Fe_3O_4/γ-Fe_2O_3) are present in the samples. On the other hand, copper ferrite can also have a spinel structure (cubic copper ferrite). Consequently, appeared spinel phase (Table 1) could be attributed to both spinel phases (iron oxides (Fe_3O_4/γ-Fe_2O_3) and cubic copper ferrite (c-$CuFe_2O_4$).

At first glance, it is not clear whether the spinel phases of iron oxide (Fe_3O_4/γ-Fe_2O_3) are present together with the c-$CuFe_2O_4$ phases up to 900°C. To draw some conclusions about the behavior of the spinel phase at temperatures below 900°C, let us recall the change in the amount of the hematite phase with the annealing temperature. The amount of the hematite phase decreases in the temperature range of 600–800°C as well as in the range of 900–1100°C.

Recall here that the spinel iron oxides undergo a phase transformation into the hematite under the annealing at temperatures higher than 600°C (Fe_3O_4/γ-$Fe_2O_3 \rightarrow \alpha$-$Fe_2O_3$) [79–82]. The crystalline sizes of hematite do not show the monotonic decrease with temperature (the size of coherent scattering domains shows the sharp increase in the amount at 900°C, Table 1) due to the presence of the spinel iron oxide phases (at the temperatures lower than 900°C), nuclei of which grow with the annealing treatment and transform into the hematite phase, under the influence of thermal treatment. For that reason, the conversion of the spinel iron oxide phases into hematite contributes to a significant increase in the amount of the α-Fe_2O_3 at 900°C. The mentioned wt % increase confirms that the phase transformation of spinel iron oxide phases to hematite is pronounced at temperatures lower than 900°C.

At temperatures higher than 900°C, the size of the α-Fe_2O_3 nanoparticles do not increase, although their amount regularly decreases with further temperature rise, due to conversion to copper ferrite. Accordingly, the decrease in the amount of hematite confirms the formation of the copper ferrite phase. The temperature range, in which cubic copper ferrite phase is formed, is difficult to determine without considering the behavior of t-$CuFe_2O_4$ phase. Unlike the spinel phase, the tetragonal $CuFe_2O_4$ phase is formed in larger quantities. Its amount and crystallite size increase regularly with heat treatment up to 1000°C. Between 1000 and 1050°C, a sharp drop in the amount of t-$CuFe_2O_4$ phase is observed, which could be explained in the terms of the technical nature, i.e., the program calculates the wt % in respect to the entire crystalline phase. On the other hand, the spinel phase is represented with the lowest amount in the examined samples, and it was the most complicate to determine exactly its wt %. Although the t-$CuFe_2O_4$ decreased for 10 wt %, and the amount of c-$CuFe_2O_4$ is increased for only 1%, the observed wt % behavior confirming the presence of the phase transformation t-$CuFe_2O_4 \rightarrow$ c-$CuFe_2O_4$ in the temperature range from 1000 to 1050°C (Table 1), which unequivocally confirms the presence of the mentioned phase transformation. The literature data confirmed that the prevalence of copper cations in the coprecipitation synthesis, performed in the same laboratory to obtain copper ferrite, leads to the structural transformation of t-$CuFe_2O_4 \rightarrow$ c-$CuFe_2O_4$, which is an important part of the copper ferrite formation mechanism [43]. Accordingly, it can be assumed that the spinel phase, observed in the investigated samples annealed at higher temperatures, can be attributed to the c-$CuFe_2O_4$ phase.

The amorphous matrix completed the phase transformation to crystalline silica at 1000°C (Figs. 1h and 1i). Cristobalite is a phase present at all annealing temperatures above 1000°C. The observed decrease in the weight fraction of quartz and cristobalite after annealing the sample to 1050°C indicates conversion of mentioned phases to the tridymite phase. Noteworthy, in the temperature range from 1050 to 1100°C, the amount of cristobalite retains the same value (Table 1), while the amount of tridymite is increased by the same amount with which the quartz phase was present at 1050°C (3 wt %, Table 1). This confirms that the entire amount of quartz has been transformed into tridymite up to 1100°C.

To represent the more transparent results classified in Table 1, the change in the amount and crystallite size of every phase, governed by thermal treatment, is shown in Figs. 2 and 3.

The changes in the amount of the presented phases and their crystallite sizes confirm the presence of phase transformations in the examined samples. According to Fig. 2, the amount of phases is changed by heat treatment for all non-silica phases until an annealing temperature of 1000°C, after which it remains practically unchanged. This is an indicator that there is no further phase transformation of the phases in the pores of the silica matrix above 1000°C. After annealing at 1000°C, crystallization of a silica matrix occurs, and further thermal treatment initiates only phase transformations of the silica matrix.

On the other hand, changes in the crystallite sizes show completely different behavior (Fig. 3), which is a consequence of the confinement of the nanoparticles within the silica pores of certain sizes. It can be noticed that the size of the coherent domains does not change significantly during heat treatment in the case of $Cu_2(OH)_3NO_3$ phases (Figs. 3a and 3b). In the case of CuO and spinel phases, crystallite sizes do not

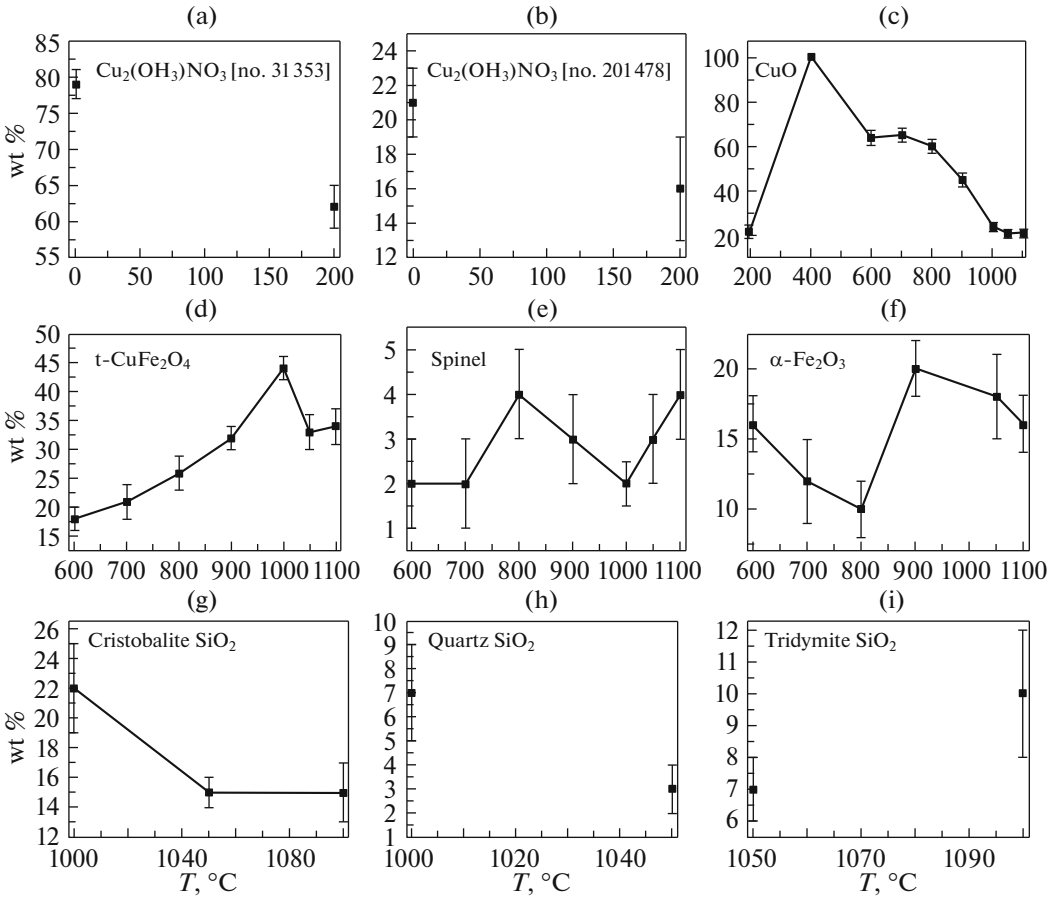

Fig. 2. Representation of thermally initiated changes of the weight fractions of the (a) $Cu_2(OH)_3NO_3$ [no. 31353] phase; (b) $Cu_2(OH)_3NO_3$ [no. 201478] phase; (c) CuO phase; (d) t-$CuFe_2O_4$ phase; (e) spinel phases; (f) α-Fe_2O_3 phase; (g) cristobalite SiO_2 phase; (h) quartz SiO_2 phase; (i) tridymite SiO_2 phase.

change more prominently after annealing at 900°C (Figs. 3c and 3e), as well after 1000°C in the case of t-$CuFe_2O_4$ and α-Fe_2O_3 phases (Figs. 3d and 3f). The alteration in the crystallite sizes of the presented phases will be further discussed in Section 4.1.

3.2. FTIR Measurements

Since the main idea of this study was to investigate the influence of thermal treatment on the formation mechanism of the phases in the pores of silica matrix, as well on the silica matrix, the surface of the samples containing different copper and iron phases (Figs. 1d–1h) was investigated by ATR-FTIR measurements. FTIR spectra of the samples annealed at temperatures (600, 700, 800, 900, 1000, 1050, and 1100°C) are represented in Fig. 4.

Presented noise in the FTIR spectra of the investigated samples (in the wavenumber range of 3980–3450 cm^{-1}, as well in the range of 2000–1300 cm^{-1}) is related to the background H_2O gas-phase spectrum. The observed vibrations are attributed to stretching and bending vibrations, respectively [83, 84]. Noise in the range of 2370–2000 cm^{-1} arose due to the presence of diamond, used as the material from which the ATR crystal is made [85]. Maximum at 2650 cm^{-1} (presented in the all measured FTIR spectra) points to the intermolecular bonded O–H groups of ethanol, used for cleaning the area of ATR crystal before measurement of FTIR spectrum of each sample [44, 86, 87].

Having in mind that significant differences in FTIR spectra can be observed in the wavelength range of 1400–400 cm^{-1}, the magnified parts of the spectra indicating the characteristic bond positions in the middle IR spectra are shown in Fig. 5.

The phase which is dominant in the spectra of Fig. 5 is silica (amorphous or crystalline phases); diversity of the crystalline silica maxima is observed in Figs. 5e–5g. Accordingly, before interpreting the FTIR spectra of nanocomposite samples containing a silica matrix, it is necessary to underline the remarks below. One of the problems related to the interpretation of the FTIR spectrum of samples consisting of

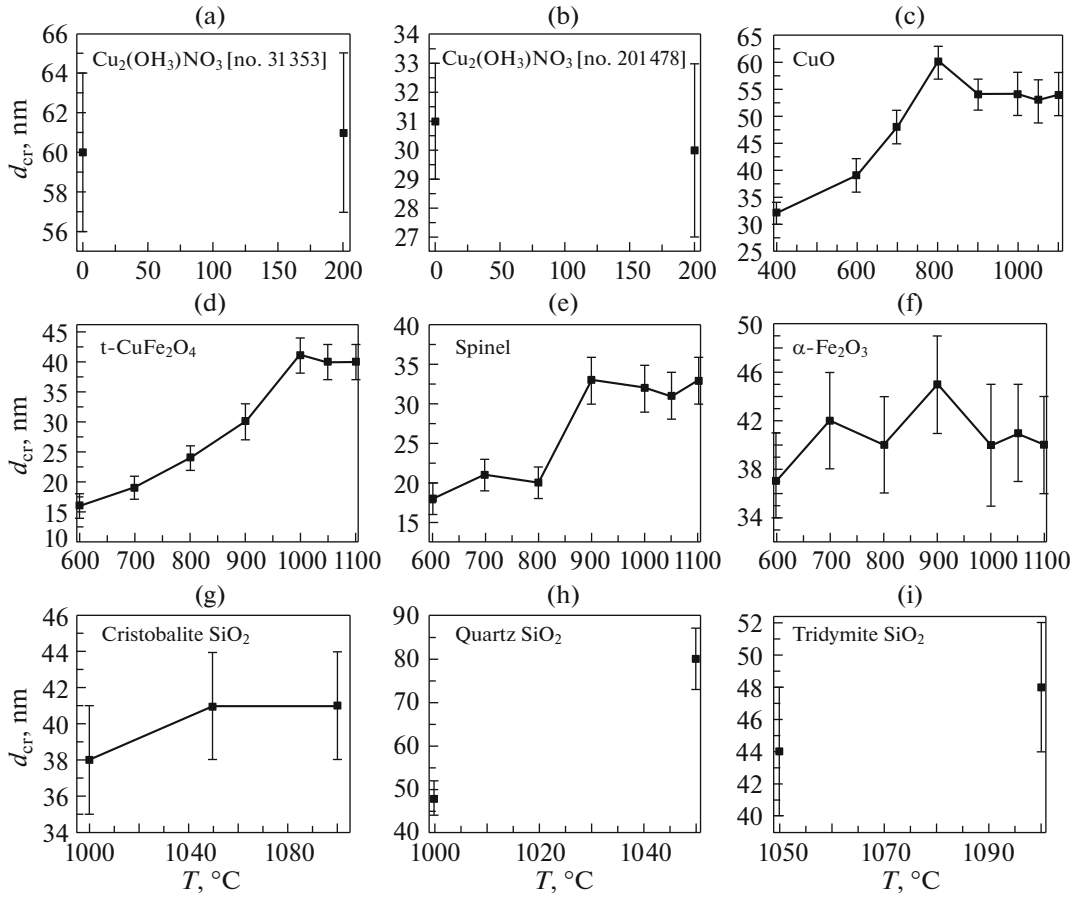

Fig. 3. Representation of thermally initiated crystallite growth of the: (a) $Cu_2(OH)_3NO_3$ (no. 31353) phase; (b) $Cu_2(OH)_3NO_3$ (no. 201478) phase; (c) CuO phase; (d) t-$CuFe_2O_4$ phase; (e) spinel phases; (f) α-Fe_2O_3 phase; (g) cristobalite SiO_2 phase; (h) quartz SiO_2 phase; (i) tridymite SiO_2 phase.

different silica polymorphs is that the identification of individual silica structures is not always simple due to the complexity of the investigated samples. As a result of the impossibility to determine precise crystal structure of the silica phases of the samples consisting of two or three silica phases, there are frequent disagreements in the literature regarding the interpretation of FTIR silica spectra. In other words, since the authors usually do not take into account the exact structure of the crystalline silica phase present in their samples, errors often occur in the classification of the vibration modes of the mentioned phase. In the cases of some silica phases, this type of error is a consequence of the lack of knowledge about the true crystal symmetry of the represented phase [88], which results in different selection rules for classification of the vibrations of the same silica phase. Consequently, non-uniform ascription of the same vibrations to different silica bonds modes can be found in literature [89–97].

The most common discrepancies appear in the case of bending vibrations, which are often clustered in the low-wavenumber range of the spectra, where the characteristic bonds of the spinel and hematite phases are also observed. With this in mind, the bending vibrations in this study are not labeled as symmetric or antisymmetric and will not be considered independently in Section 4.2.

Noteworthy, Fig. 5 revealed that in the FTIR spectra of the investigated samples, a higher number of stretching vibrations, characteristic for the silica phase, is observed than the number of characteristic bending vibrations of the silica phase. In our opinion, bending vibrations (appeared as a result of changes in bond angles, which usually precede the change in the bond length, characterized by the stretching vibrations), are rarely observed (in comparison with the number of the observed stretching vibrations) in the FTIR spectra of prepared samples due to large steps in temperature increase during annealing treatment; i.e., the authors assume that performing heat treatment by annealing the samples in much smaller steps (for example, instead of increasing the temperature by 100°C, to increase the temperature by 10°C) would

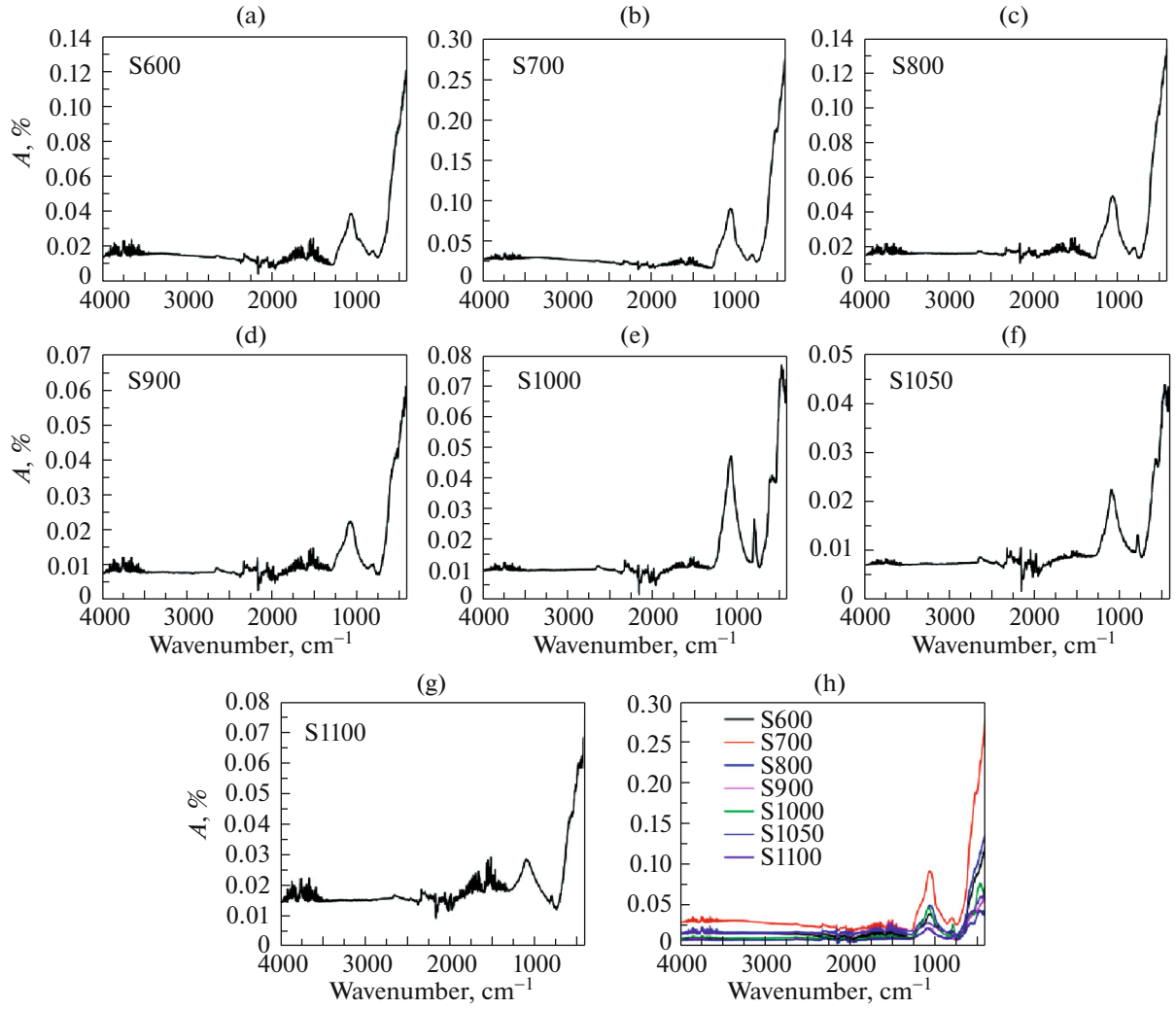

Fig. 4. Room-temperature FTIR spectra of the samples: (a) S600; (b) S700; (c) S800; (d) S900; (e) S1000; (f) S1050; (g) S1100; and (h) FTIR spectra of the all investigated samples presented at the same graph.

allow more bending vibrations, characteristic for silica phase, to be observed.

Figure 5a represents the FTIR spectrum of the sample S600. At the higher wavenumber end, vibrations characteristic for silica matrix are presented. Asymmetric and symmetric stretching vibrations of Si–O–Si bridging oxygen groups numbered (1) and (3) could be observed at 1063 and 805 cm^{-1}, respectively [88, 89]. At 969 cm^{-1} (2), asymmetric stretching of Si–OH silanol groups (ν_{as} Si–OH) occurs [98, 99], although this position could also be characteristic for asymmetric stretching of non-bridging oxygen (ν_{as} Si–O) [98–100], which is often recognized in the literature as silanol free broken bonds (Si–O). The presence of this vibration is also observed in the FTIR spectrum of the sample S700 (Fig. 5b). According to literature data, the disappearance of silanol bonds up to 800°C (FTIR spectrum of the S800 confirms this fact, Fig. 5c) is predicted.

Vibrations in the low-wavenumber part of the FTIR spectra are difficult to attribute unequivocally to certain vibrations of one phase in the investigated nanocomposite samples, because in this part of the FTIR spectrum, characteristic vibrations of the Fe–O bonds are present. Further, bending O–Si–O vibration is observed as a shoulder in the range 400–600 cm^{-1} [97]. As well, in this part of the spectrum, characteristic vibrations of the CuO phase appear.

Consequently, the vibrations of all mentioned phases can be observed in this part of the FTIR spectrum of the investigated samples, which will be discussed in more detail below.

It could be found in the literature that characteristic vibrations of CuO nanostructure could be observed in the range of 500–700 cm^{-1} [101]. Cu–O vibrations

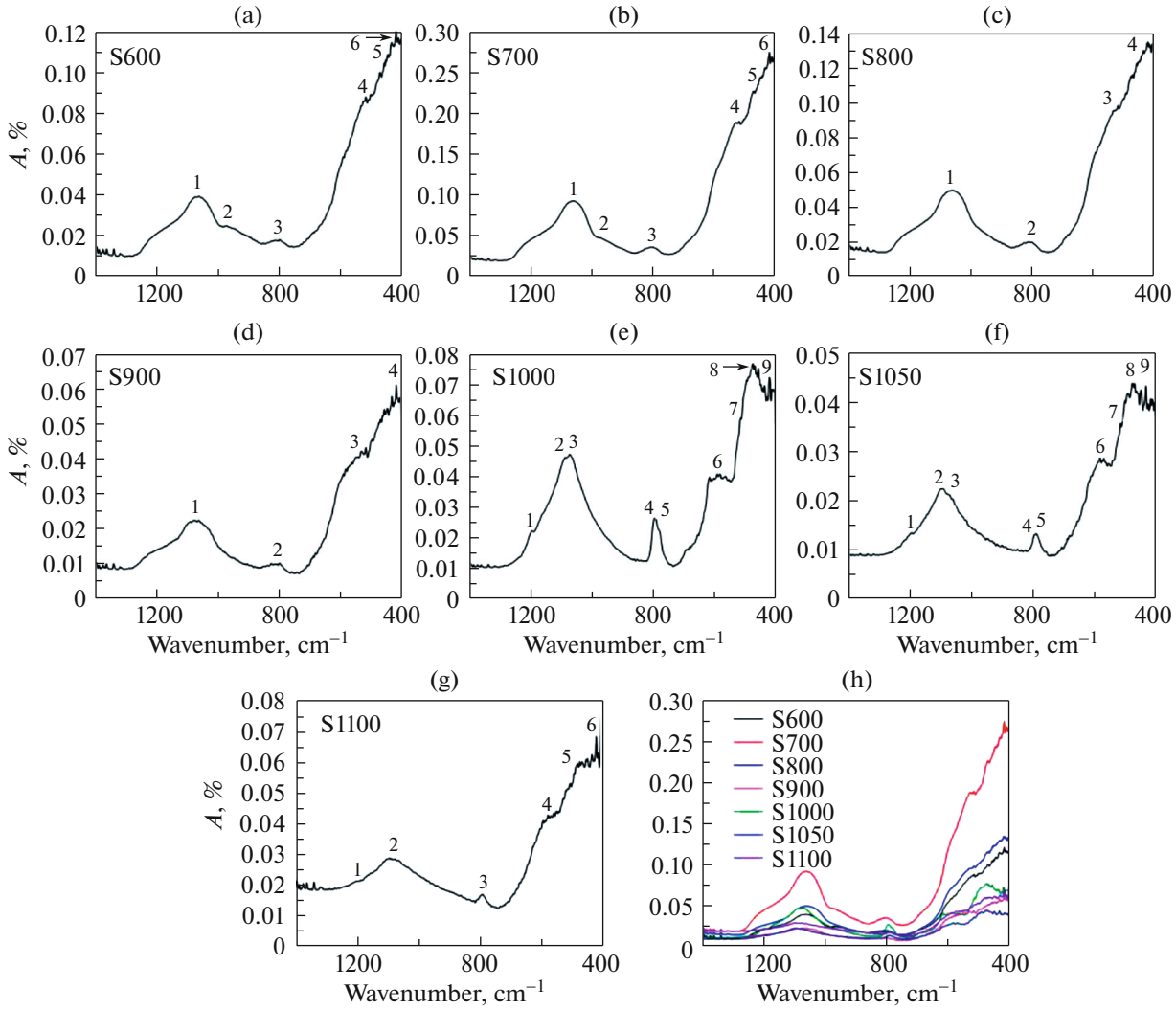

Fig. 5. FTIR spectra of the samples: (a) S600; (b) S700; (c) S800; (d) S900; (e) S1000; (f) S1050; (g) S1100; and (h) FTIR spectra of the all investigated samples presented at the same graph, in the wavenumber range: 1400–400 cm^{-1}.

at 525 cm^{-1} (observed in the FTIR spectrum of sample S600), as well as at 580 cm^{-1} (observed in the FTIR spectrum of sample S900), are attributed to the asymmetric stretching vibration of Cu–O bonds, while Cu–O vibration centered between 450–410 cm^{-1} is attributed to a symmetric mode of Cu–O stretching vibration [102, 103]. The observed vibration at 473 cm^{-1} may indicate a shifted stretching vibration Cu–O in the direction of higher wavenumbers, which indicates a change in the bond length and the presence of a phase transformation [104]. Also, vibrations at 525, 473, and 415 cm^{-1} could be ascribed to Fe–O bonds from the cubic copper ferrite phase [104, 105]. Note that the observed vibration at 525 cm^{-1} could be ascribed to the shifted vibration of the tetrahedral Cu^{2+} cations of $CuFe_2O_4$, i.e., to the Cu–O bond [43, 104]. As well, vibration at 525 cm^{-1} could be attributed to the Fe–O bond from the iron oxide spinel phase(s) in the case of FTIR spectra of the samples S600–S900 (this conclusion is supported by the fact that the amount of hematite phase was increased at 900°C, XRD analysis (Table 1) [43, 104]). And, the literature data confirm that the mentioned vibration is characteristic for Fe–O bond vibrations of α-Fe_2O_3 [106, 107]. Noteworthy, vibrations at 525 and 473 cm^{-1} could be ascribed to bending bonds of silica matrix [97]. In summary, broad minima at 525 and 473 cm^{-1} are characteristic for Si–O–Si bending vibrations of SiO_2, for the Fe–O and Cu–O vibrations of copper ferrite phases, as well as for Fe–O bond vibrations of iron oxide phases. Having in mind that the diffraction patterns revealed the presence of all mentioned phases in samples annealed in the temperature range from 600 to 1000°C, broad minimum could point to the superposition of the vibrations characteristic for all

observed compounds (Fig. 5): silica matrix, copper ferrite phase, and iron oxide phases. Discussed vibrations are shifting, with thermal treatment, since the phase ratio and crystallite size of presented phases are altered by annealing treatment. Also, it is important to note that these vibrations, appeared in the low-wavenumber part of the spectrum, are characteristic for mentioned phases and present in the FTIR spectra of all the investigated samples.

FTIR spectrum of the sample annealed at 700°C (Fig. 5b) revealed the presence of the same vibrations observed in the sample S600. The vibrations at 1063 (1), 805 (3), 473 (5), and 415 cm^{-1} (6) are at the same wavenumber as in the case of sample S600 (vibrations are not shifted); i.e., the same positions of the four vibrations indicate that the length of the mentioned bonds has not changed after heat treatment in the temperature range from 600 to 700°C. Also, the shift of the vibrations labeled (2) and (4) confirmed nanoparticle growth.

Note that the FTIR spectrum of the sample S700 (Fig. 5b), showed significantly higher absorption of the infrared radiation compared with other investigated samples (Fig. 5h). The origin of the increased absorption could be of very technical nature. The appearance of the air, between the sample and the diamond, could weaken absorbance signal.

On the other hand, literature data revealed that different types of inhomogeneity within the sample also could influence the intensity of the absorbance signal [108]. Here, it should be recalled that absorption of IR radiation in the range from 400 to 1400 cm^{-1} required interaction of the oscillating electric field of appropriate radiation with the molecule's bond. This interaction is made possible by the change in the dipole moment of the molecule, which occurred during the vibration of the molecule. Energy absorption occurs when the vibration frequency of the bond is equal to the vibration frequency of the electromagnetic field. The mentioned interaction induces bending and stretching motion of the bond of the molecule (see Discussion), characterized by a certain value of the dipole moment. Since the dipole moment represents, mathematically, a product of the magnitude of the separated charge and the distance between considered charges, the change in the magnitude of the second value (distance) points to the fact that the change in the dipole moment could be used to investigate structural changes within the examined material. Accordingly, the increased absorption of the sample S700 may indicate that the sample contains a significantly higher number of inhomogeneities (such as vacancies, for example). Furthermore, if we now consider that the FTIR spectrum of the sample S800 showed the lowered number of vibrations (vibrations numbered (2) and (5) at Fig. 5a are missing in Fig. 5c), increased absorption intensity of the sample S700 is depicting to the more prominent changes of the structure of silica matrix, which paves the path to the disappearance of two bonds presented in the FTIR spectra of the samples S600 and S700 (silanol (2) and bending O–Si–O (5) bonds). These structural changes of the amorphous silica matrix cannot be observed by XRD measurements, and result in changes of the SiO_2 pore size, which affects the phase transformation of the phases within the silica pores. Namely, the FTIR spectrum of S800 confirms more pronounced changes in the symmetry of the sample S800 (compared to the S600 and S700 samples); bearing in mind the correlation between symmetry and structure [109], samples S700 and S800 have the distinctly different structure, although their phase composition is the same (Table 2). Monitoring of the silica matrix structural changes by FTIR measurements will be commented in Section 4.2.

Table 2. The change of the absorption ratio of the characteristic peaks of the crystalline quartz

Sample	Calculated ratio
S1000	1.66
S1050	1.03

FTIR of the sample S900 is presented in Fig. 5d, and it could be noticed that this spectrum is more significantly similar to the spectrum of the sample S800, consisting of the same number of the observed, slightly shifted vibrations (stretching Si–O–Si, stretching Fe–O, and bending Cu–O). The shift could point to the structural changes within the sample, induced by annealing treatment. In this FTIR spectrum, only one vibration is present, at the same wavenumber position as in the case of the sample annealed at 800°C, and this is the stretching Si–O–Si vibration (labeled with no. (2)). This confirms the higher degree of densification of the silica matrix in the temperature range of 800–900°C.

On the other hand, the FTIR spectrum of the sample S1000 (Fig. 5e) confirmed the crystallization of the amorphous silica matrix at 1000°C (Table 2) and the appearance of crystalline silica polymorphs. Figure 5e showed variations in the number of the observed bonds, as well as in their positions, in comparison with FTIR spectra of the samples annealed at lower temperatures; i.e., this FTIR spectrum contains the same vibrations observed in the spectrum of S900, although the additional bonds, the presence of which is confirmed by vanishing of amorphous silica and further crystallization of silica matrix, could be observed. Figure 5e revealed the small minimum at 1198 cm^{-1}, ascribed to symmetric Si–O stretching vibration [110]. Minimum positioned at 1090 cm^{-1} is related to the asymmetric Si–O stretching vibration [110], while the minimum at 1073 cm^{-1} could be attributed to the stretching vibration of the Si–O–Si bridging oxygen [96]. Minimum at 796 cm^{-1} is assigned to the Si–O–Si

Table 3. FTIR stretching (ν) and bending (δ) vibrational bonds for the sample S600

S600			
Bond number	$\tilde{\nu}$ of vibration, cm^{-1}	Mode of vibration	Ref.
1	1063	ν_{as}(Si–O–Si)	[88]
2	978	Si–O free broken; ν_{as}(Si–OH)	[87]
3	805	ν_s(Si–O–Si)	[89]
4	525	$\nu_s(Fe–O)_A$; ν_{as}(Cu–O); δ(Si–O–Si); δ(Fe–O)	[96, 97, 100, 101, 104, 116]
5	473	ν_s(Cu–O); δ(O–Si–O); $\nu(Fe–O)_B$	[44, 101, 104]
6	415	ν_s(Cu–O); $\nu(Fe–O)_B$	[96, 97, 101, 104]

bending vibrations [110]. A small minimum at 697 cm^{-1} indicates the presence of a spinel phase [111], which is attributed to the symmetric bending mode of the tetrahedral unit within the spinel lattice (Fe–O vibration) [104].

Recall that we assumed that the phases of spinel iron oxide were not present in the system after its final conversion to hematite at 900°C (Table 1). Since c-$CuFe_2O_4$ represents an inverse spinel, in which Cu^{2+} cations occupy only octahedral sites (B cation positions), while half of Fe^{3+} cations are statistically distributed in the octahedron, and the half at tetrahedral sites (A cation positions) [44], the observed vibration at 697 cm^{-1} (685 cm^{-1}) can be attributed to bending Fe–O vibration from the c-$CuFe_2O_4$ phase [104]. Also, literature recognized vibration at 697 cm^{-1} as the maxima characteristic for alpha quartz [112]. The other peaks characteristic for alpha quartz are doublet maxima, observed at 779–780 and 790–798 cm^{-1} [113]. Accordingly, the mentioned vibrations could be attributed to the quartz phase. On the other hand, the cristobalite phase has maxima at similar wavenumber positions as quartz, although the appearance of doublets is not characteristic for cristobalite [88]. It should be noted that the bending Si–O–Si vibration, characteristic for amorphous silica (appears at lower wavenumbers), disappears at 1000°C [111], which indicates the crystallization of the silica matrix.

The FTIR spectrum of the sample S1050 (Fig. 5f) showed maxima at very similar positions, as in the case of sample S1000, with the difference that maximum at 697 cm^{-1}, which was observed for the sample S1000, is present in this spectrum as almost negligible visible shoulder, shifted to the lower wavenumbers (685 cm^{-1}). The shift to the lower wavenumbers confirms the increased mass of the sample (vibration frequency is inversely proportional to the mass), which is expected, since after annealing the sample at 1050°C, another silica crystalline phase, tridymite, appeared (see Section 3.1).

Also, confirmation of the further crystallization of silica matrix at higher temperatures could be found in the shift and change of the absorption ratio of the characteristic peaks of one of the present SiO_2 polymorphs—crystalline quartz phase in the FTIR spectra of the samples S1000 and S1050. The ratio of the absorption around 800 cm^{-1} (in our case, the mentioned vibration is positioned at 796 and 794 cm^{-1} for the samples annealed at 1000 and 1050°C, respectively) and absorption around 695 cm^{-1} (vibration at 697 and 685 cm^{-1}, in the samples S1000 and S1050, respectively), provides information on the degree of crystallinity of one of the silica phases [114, 115]. Results are shown in Table 2.

Accordingly, FTIR measurements enable the confirmation of the growth of quartz nanoparticles (both peaks are shifted in the direction of the lowered wavenumbers), as well as an increase in crystallinity (the increase of the annealing temperature results in a reduced value of the calculated ratio) of the quartz phase.

Figure 5g shows the FTIR spectrum of the sample S1100, which is characterized by a smaller number of observed vibrations, compared to FTIR samples S1000, and S1050, although the formation of new bonds was not observed, see more in Section 4.2.

For a better overview of the data, experimentally observed positions of absorption maxima, found in the FTIR spectra of the investigated samples, are presented in Tables 3–9.

3.3. Electrochemical Characterization

Electrochemical characterization of three chosen Fe and Cu-containing samples (S, S800, and S1100) was performed to gain deeper insight into the behavior of the studied nanocomposite systems. Figure 6 shows cyclic voltammograms (CVs) of S, S800, and S1100 electrodes in 1 M KOH (N_2-saturated), recorded at 25 mV s^{-1} and room temperature.

The anodic current peaks a_1 and a_2, at around –0.85 and –0.65 V, Fig. 6 correspond to the iron oxidation to Fe(II), and Fe(II) to Fe(III), respectively [117]. For the sample S800, these peaks are less noticeable than for the sample S because of the overlapping with broad and more intense peak a_3 (Fig. 6). On the

Table 4. FTIR stretching (ν) and bending (δ) vibrational bonds for the sample S700

S700			
Bond number	$\tilde{\nu}$ of vibration, cm^{-1}	Mode of vibration	Ref.
1	1063	ν_{as}(Si–O–Si)	[88]
2	969	Si–O free broken; ν_{as}(Si–OH)	[87]
3	805	ν_s(Si–O–Si)	[89]
4	519	$\nu_s(Fe–O)_A$; ν_{as}(Cu–O); δ(Si–O–Si); δ(Fe–O)	[96, 97, 100, 101, 104, 116]
5	473	ν_s(Cu–O); δ(O–Si–O); $\nu(Fe–O)_B$	[44, 101, 104]
6	415	ν_s(Cu–O); $\nu(Fe–O)_B$	[96, 97, 101, 104]

Table 5. FTIR stretching (ν) and bending (δ) vibrational bonds for the sample S800

S800			
Bond number	$\tilde{\nu}$ of vibration, cm^{-1}	Mode of vibration	Ref.
1	1056	ν_{as}(Si–O–Si)	[88]
2	811	ν_s(Si–O–Si)	[89]
3	532	$\nu_s(Fe–O)_A$; ν_{as}(Cu–O); δ(Si–O–Si); δ(Fe–O)	[96, 97, 100, 101, 104, 116]
4	440	ν_s(Cu–O); $\nu_s(Fe–O)_B$	[96, 97, 101, 104]

Table 6. FTIR stretching (ν) and bending (δ) vibrational bonds for the sample S900

S900			
Bond number	$\tilde{\nu}$ of vibration, cm^{-1}	Mode of vibration	Ref.
1	1074	ν_{as}(Si–O–Si)	[88]
2	811	ν_s(Si–O–Si)	[89]
3	580	$\nu_s(Fe–O)_A$; ν_s(Cu–O); δ(Si–O–Si); δ(Fe–O)	[96, 97, 101, 104, 116]
4	452	ν_s(Cu–O); $\nu_s(Fe–O)_B$	[96, 97, 101, 104]

Table 7. FTIR stretching (ν) and bending (δ) vibrational bonds for the sample S1000

S1000			
Bond number	$\tilde{\nu}$ of vibration, cm^{-1}	Mode of vibration	Ref.
1	1198	ν_{as}(Si–O–Si)	[97, 99]
2	1090	ν_{as}(Si–O–Si)	[97, 99]
3	1074	ν_{as}(Si–O–Si)	[86]
4	796	ν_s(Si–O–Si)	[97, 99]
5	790	ν_s(Si–O–Si)	[106, 108]
6	697	δ(Si–O); ν(Fe–O)	[104]
7	579	$\nu_s(Fe–O)_A$; ν_{as}(Cu–O); δ(Fe–O)	[100, 101, 104, 116]
8	476	ν_s(Fe–O); ν_s(Cu–O)	[44, 101, 104]
9	427	ν_s(Cu–O); $\nu(Fe–O)_B$	[96, 97, 101, 104]

other hand, two well-defined anodic peaks, a_3 and a_4, observed for S and S800 samples at −0.46 and approximately −0.2 V, can be ascribed to the oxidation from Cu(0) to Cu(I) and from Cu(I) to Cu(II), respectively [118, 119]. In the case of S800, the a_3 and a_4 peaks are less intense, but broader comparing with S, which can

Table 8. FTIR stretching (ν) and bending (δ) vibrational bonds for the sample S1050

S1050			
Bond number	$\tilde{\nu}$ of vibration, cm^{-1}	Mode of vibration	Ref.
1	1198	ν_{as}(Si–O–Si)	[97, 99]
2	1090	ν_{as}(Si–O–Si)	[97, 99]
3	1070	ν_{as}(Si–O–Si)	[86]
4	796	ν_{s}(Si–O–Si)	[97, 99]
5	790	ν_{s}(Si–O–Si)	[108]
6	685	δ(Si–O); ν(Fe–O)	[104]
7	585	ν(Fe–O)$_A$; ν_{as}(Cu–O); δ(Fe–O)	[100, 101, 104, 116]
8	476	ν_{s}(Fe–O); ν_{s}(Cu–O)	[44, 101, 104]
9	421	ν_{s}(Cu–O); ν(Fe–O)$_B$	[96, 97, 101, 104]

Table 9. FTIR stretching (ν) and bending (δ) vibrational bonds for the sample S1100

S1100			
Bond number	$\tilde{\nu}$ of vibration, cm^{-1}	Mode of vibration	Ref.
1	1198	ν_{as}(Si–O–Si)	[97, 99]
2	1090	ν_{as}(Si–O–Si)	[97, 99]
3	790	ν_{s}(Si–O–Si)	[97, 99]
4	576	ν(Fe–O)$_A$; δ(Fe–O); ν_{as}(Cu–O)	[100, 101, 104, 116]
5	440	ν_{s}(Fe–O)$_B$; ν_{s}(Cu–O)	[96, 97, 101, 104]
6	419	ν_{s}(Cu–O); ν(Fe–O)$_B$	[96, 97, 101, 104]

be explained by the presence of various crystalline phases in the sample S800 (Table 1), resulting in wider distribution of electron transfer rate constants [120] than in the sample S. Anodic peak a_5, at around 0.4 V, can be related to iron [117]. Namely, in strong alkaline environment, soluble FeO_2^- can be formed and further oxidized, at higher potentials, to ferrate(IV) and ferrate(VI) species [117], which in the case of S800 corresponds to the a_5 peak. In the presence of silicate, silico-ferrate(VI) can be formed through partial replacement of Fe^{6+} with Si^{4+} occurring due to the isomorphism between the tetrahedral anions FeO_4^{2-} and SiO_4^{4-} and cations Si^{4+} and Fe^{6+} [117]. The absence of the a_5 peak in voltammogram of the sample S can be a consequence of the presence of nitrate ions in the immediate vicinity of Fe(III), which could have an inhibitory effect on the further oxidation [121].

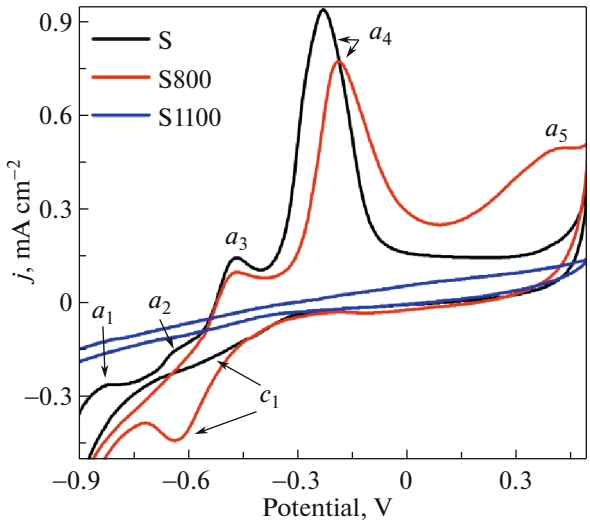

Fig. 6. Cyclic voltammograms of S, S800, and S1100 electrodes in 1 M KOH (N_2-saturated), at 25 mV s^{-1}.

In a cathodic direction, the c_1 peak, observed in the potential range from –0.5 to –0.6 V, can be ascribed to Cu(II) reduction [122]. In fact, the Cu(II) species formed during the a_4 oxidation include CuO, $Cu(OH)_2$, and $Cu(OH)_4^{2-}$. The c_1 peak is supposed to be predominantly due to the reduction of CuO to metallic copper [122]. The presence of CuO in the electrode material S800 itself (Table 1) makes this peak more intense for the sample S800 than for the S.

The oxidation/reduction peaks of S and S800 can hardly be observed in the case of the sample S1100 as a consequence of crystallization of SiO_2 phases at high annealing temperatures. Let us recall that Cu and Fe-containing crystalline grains are placed in the pores of the silica matrix. As a result of SiO_2 crystallization, most of the Cu and Fe-containing grains become surrounded by dense SiO_2 layers, which makes them isolated and prevents the OH^- ions diffusion [117] towards these grains.

4. DISCUSSION

4.1. XRD Discussion

This section will consider the influence of the temperature gradient acting on the sample in the furnace on the phase transformations and geometric distribution of the phases in the sample. Since the T_{grad} changes significantly in time, we will consider heating the sample in the first moment, when the desired temperature in the furnace is reached. In these circumstances, the presence of T_{grad} in respect to the increase in sample thickness is shown in Fig. 7.

Figure 7a represents a bird's eye view on the annealed powder in the crucible with a spherical bottom. If we imagine that we divide the sample with two lines, we can propose that all divided parts of the sample are characterized by the same depth profile, represented as solid-filled intercept, and Fig. 7b shows this intercept enlarged. Figure 7b does not show a bird's eye view of the intersection of the annealed powder, but the depth profile, in order to present the influence of T_{grad} on the sequence of occurrence of phase transformations and change of the phase distribution in the sample, with the thickness of the sample.

In the first moment of the heating, the T_{grad} is the highest at the surface of the sample, because of the heat distribution in the furnace, as well as because of the heat transfer through the annealed sample. The heaters are placed in such a way that the sample is evenly heated, which means that the heat reaches the deeper parts of the sample volume more slowly ($T - dT$), compared to the surface part, due to a certain thickness of the sample. Accordingly, in the first moment of heating, the deeper volume of the sample will have a lower temperature than the surface; i.e., the internal volume of the sample closer to the surface is exposed to a higher temperature compared to the parts of the volume that are further away from the sample surface. The central part of the intrinsic volume of the sample (which is the most distant from the surface) will be exposed to the lowest temperature of the T_{grad} acting on the sample. T_{grad} determines the occurrence of the phase transformations, and, consequently, the geometrical distribution of the presented phases, along the sample volume (Fig. 7).

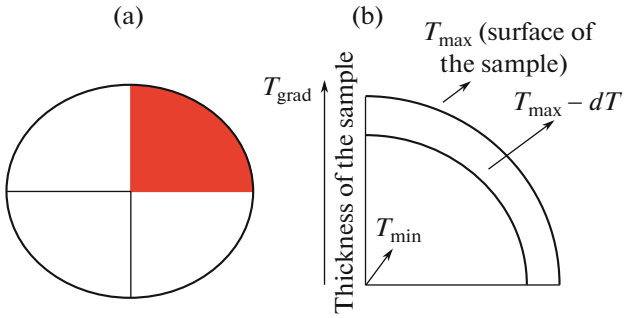

Fig. 7. (a) A bird's eye view on the sample in the annealing crucible (geometrical representation); (b) depth profile of the solid-filled intercept of (a) intersection of the annealed sample, in respect to the change of its thickness, view from the surface (T_{max}) to the centre of the sample (T_{min}).

Dependent on these two parameters (T_{grad} and T_{ann}), the amounts and crystalline sizes of the presented phases vary for each sample, as well for each silica pore, individually. The silica pores represent a part of the volume of the sample, which is characterized by a certain depth. In the case of a T_{grad} acting on the pores of a silica matrix, it can be assumed that it is highest on the pore surface, while the temperature in the middle of the pore volume is the lowest. Nevertheless, to simplify, we can assume that the differences between the pores in the sample annealed at the same temperature are not too pronounced.

To understand the influence of T_{grad} on the phase transformations and the phase distributions of the investigated samples, let us recall that, according to Section 3.1, proposed reactions, involved in the formation mechanism of the investigated samples, are:

$Fe_3O_4/\gamma\text{-}Fe_2O_3 \rightarrow \alpha\text{-}Fe_2O_3$ (occurred within the T range of 600–1000°C),

$\alpha\text{-}Fe_2O_3 + CuO \rightarrow t\text{-}CuFe_2O_4$ (occurred within the T range of 600–1100°C),

$t\text{-}CuFe_2O_4 \rightarrow c\text{-}CuFe_2O_4$ (occurred within the T range of 1000–1050°C),

amorphous $SiO_2 \rightarrow$ cristobalite SiO_2 (occurred within the T range of 900–1000°C),

cristobalite $SiO_2 \rightarrow$ quartz SiO_2 (occurred within the T range of 1000–1050°C),

cristobalite $SiO_2 \rightarrow$ tridymite SiO_2 (occurred within the T range of 1000–1050°C),

quartz $SiO_2 \rightarrow$ tridymite SiO_2 (occurred within the T range of 1050–1100°C).

Taking into account these reactions, we can get a deeper insight into the influence of temperature on the mechanism of formation and geometrical distribution of the phases in silica pores, as well as on the geometrical distribution of crystalline silica phases, in the samples annealed at temperatures above 1000°C. The CuO phase is present in the largest amount in the

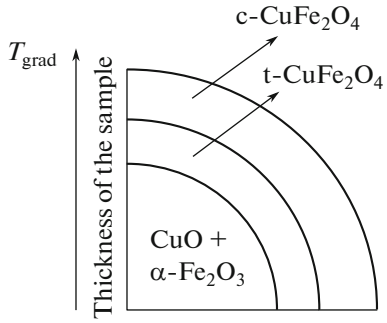

Fig. 8. Intersection of the pore of the samples S1000, S1050, and S1100 (depth profile), and the phase distribution in the pore of the sample, in respect to the change of its thickness (view from the surface to the centre of the pore).

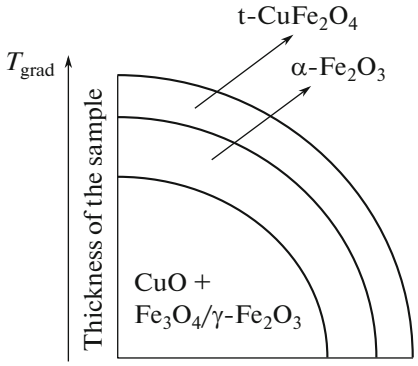

Fig. 9. Intersection of the pore of the samples S600, S700, S800, and S900 (depth profile), and the phase distribution in the pore of the sample, with respect to the change of its thickness (view from the surface to the centre of the pore).

investigated samples. It is also observed in all samples annealed in the temperature range from 200 to 1100°C (Table 1). Due to the influence of the T_{grad}, it can be assumed that the CuO nanoparticles closer to the surface are consumed in the formation reactions of other compounds ($CuFe_2O_4$). The CuO in the deeper volume of the sample is not exposed to any phase transformation. The similar can be observed in the case of crystalline silica matrix phases. Cristobalite is the crystalline phase of silica, present in the largest amount in all samples consisting of crystalline silica matrix (S1000–S1100, Table 1). Cristobalite nanoparticles closer to the surface are converted to quartz and tridymite, while cristobalite in the deeper sample volume is retained in the same phase. This will be discussed in more detail below.

Analysis of the behavior of the phases in the pores of the silica matrix revealed that the occurrence of t-$CuFe_2O_4$ → c-$CuFe_2O_4$ transformation requires almost the highest temperatures (Section 3.1). Consideration of the presence of T_{grad} brings to the conclusion that the c-$CuFe_2O_4$ appears in the closest vicinity to the surface of the pore. In the deeper volume of the pore, t-$CuFe_2O_4$ is placed, which does not experience structural conversion due to the presence of T_{grad}, and a lowered temperature that acts on the deeper volume of the annealed sample (Fig. 7).

In the samples annealed at 900 and 1000°C, α-Fe_2O_3 and CuO nanoparticles are located deeper in the pore volume. Figure 8 presents a simplified illustration of the proposed geometrical distribution of the phases (view from the surface to the centre of the sample).

The geometrical distribution of the phases within the silica pores is not changed more significantly with thermal treatment above 1000°C (except for the case of t-$CuFe_2O_4$ → c-$CuFe_2O_4$ between 1000 and 1050°C, which is structural transformation), because the nanoparticles do not have enough space to grow further with thermal treatment, due to the crystallization of the silica matrix (Section 3.1).

In the case of the samples annealed in the temperature range from 600 to 900°C, the phase distribution within the silica pores is relatively similar, with the difference that we proposed that the spinel phases, observed in these samples, are ascribed to iron oxide spinel phases, i.e., that phase transformation t-$CuFe_2O_4$ → c-$CuFe_2O_4$ has not yet occurred. The scheme of geometrical distribution of phases within silica pores is presented in Fig. 9.

The phase transformations of the crystal silica matrix and their distribution in the samples, with respect to the change in the sample thickness, can also be explained in the term T_{grad}. Recall that cristobalite represents a phase, which is present in a larger amount than quartz and tridymite at all annealing temperatures (Table 1). Consequently, this phase is involved in the formation of quartz and tridymite.

Since the phase transformation was initiated by the elevated temperature (T_{grad}), it can be concluded that the cristobalite nanoparticles at the surface of the samples (or in the immediate vicinity of the surface) are exposed to phase transformations to quartz or tridymite. Due to the T_{grad} and thermal treatment at higher annealing temperatures, quartz transforms into the tridymite phase, which also appears at the surface of the sample.

The mentioned explanation is confirmed by the FTIR measurements (Section 3.2). FTIR is a surface technique that has made it possible to observe a higher number of maxima attributed to quartz than to cristobalite, despite the higher amount of cristobalite present in the samples S1000 and S1050 (Figs. 5e and 5f). The sequence of phase transformations of the crystalline silica matrix, which is induced by the exposure of the crystalline silica nanoparticles to the thermal treatment, and which is determined by the presence of T_{grad}, is given in Fig. 10.

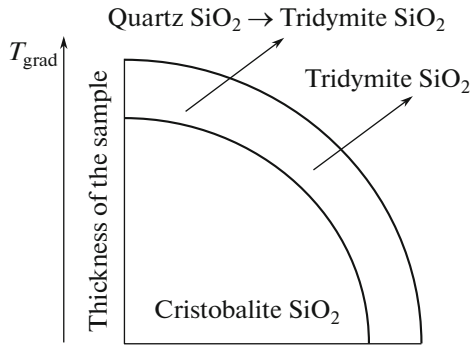

Fig. 10. Intersection of the sample S1000, S1500, and S1100 (depth profile), and the phase distribution of the crystalline silica phases in the sample, in respect to the change of its thickness (view from the surface to the centre of the pore).

Recall that Figs. 7–10 provide an understanding of the influence of T_{grad} on phase transformations, which are triggered by the growth of nanoparticles under elevated annealing temperatures. Although the samples were annealed for 3 h and 30 min at a chosen temperature, the first moment of the exposure of the sample to the selected annealing temperature induces the appearance of the T_{grad} acting on the sample, which initiates more pronounced growth of the surface nanoparticles, compared to the particles in the deeper sample volume. This process determines the sequence of the phase transformations in the sample.

4.2. FTIR Discussion

The structural changes of the silica matrix under heat treatment will be considered in this section. Since FTIR is a complementary technique to XRD measurements, analyses of the FTIR vibration behavior of the silica matrix will provide a deeper insight into the phase and structural changes within the samples initiated by the annealing treatment.

The main principle of FTIR measurement is based on the fact that IR absorption causes stretching and bending of vibrations of molecules presented in the tested samples. In the FTIR spectra of the investigated samples, stretching (bonding), ν, and deformation (bending) vibrations, δ, are observed [123]. Furthermore, the stretching vibrations induce changes in bond length while bending vibrations change bond angles, but bond lengths remain unchanged [123]. It can be noticed that the thermal treatment induces the break of certain bonds, as well as the formation of new bonds (Section 3.2). This process is enabled by the alterations of bond angles and length of the bonds, resulting in the change of the structure of the investigated material. In this way, the measured FTIR data provide a deeper insight into the structural and phase transformations of the silica. The silica matrix is changed by annealing treatment by redirecting the SiO_4 tetrahedron with a non-uniform connection of Si–O bonds, which brings the structural changes and crystallization of the silica matrix [124]. The change of the matrix affects the phase transformations of the phases present in the pores of the silica matrix.

Having in mind that crystallization of the amorphous silica matrix and presence of different silica phases are already confirmed by XRD measurements, and that XRD analysis depicted to the precise temperatures at which phase transformation of crystalline silica phases present within the investigated samples occurred, the values of the full maximum widths (FVHM) of the corresponding absorption maxima of the FTIR spectra (Fig. 5) could be used as a measured parameter for the estimation of the crystallinity of a SiO_2 matrix, i.e., for tracking the structural transformation of silica matrix with annealing procedure. Amorphous silica is characterized by the broader and less sharp maxima, which indicated a higher degree of structural disorder of the matrix (FWHM increase with the structural disorder, and vice versa); accordingly, the increase in crystallinity is reflected in the FWHM decrease. This is in accordance with Fig. 5: it is obvious that the presence of amorphous silica in the samples S600–S900 results in a more pronounced similarity of the FTIR spectrum of the samples annealed at 600–900°C (Figs. 5a–5d). Also, samples annealed within the temperature range from 1000 to 1100°C (S1000–S1100) contained crystalline silica polymorphs (characterized by narrower, higher peaks), and consequently, showed pronounced similarities in the FTIR spectra (Figs. 5e–5g).

To get a deeper insight into the behavior of asymmetric and symmetric stretching vibrations, which is important for understanding the structural and phase transformations of the silica matrix under heat treatment, the mentioned silica phase vibrations are classified in Tables 10 and 11. Also, the FWHM of the corresponding absorption maxima observed in Fig. 5 are given in these tables, with the aim of monitoring the densification of the silica matrix. FWHM values were determined manually, although the deconvolution of the peaks was performed in the case when it is impossible to find FWHM, due to the presence of two crystalline silica phases in the same sample (the peaks overlap near the same wavenumber position).

The peaks attributed to the asymmetric Si–O–Si bond, as well as its behavior with annealing treatment (Table 10), will be commented. Afterward, peaks ascribed to symmetric Si–O–Si bond (Table 11) will be discussed. Also, the peaks of amorphous silica (S600–S900, Fig. 5) will be commented on first, followed by the comments on the behavior of the peaks of crystalline forms of silica (S1000–S1100) in the text below.

According to Table 10, peak (1) of amorphous silica is characterized by the highest FWHM values

Table 10. FWHM of the bond ν_{as} (Si–O–Si), observed in the samples annealed at 600, 700, 800, 900, 1000, 1050, and 1100°C

T_{ann}, °C	ν_{as}(Si–O–Si), cm^{-1}	FWHM, cm^{-1}
600	1065 (1)	176
	978 (2)	62
700	1062 (1)	159
	969 (2)	47
800	1056 (1)	155
900	1074 (1)	177
1000	1073 (3)	151
	1090 (2)	83
1050	1075 (3)	234
	1095 (2)	87
1100	1090 (2)	190

Table 11. FWHM of the bond ν_s (Si–O–Si), observed in the samples annealed at 600, 700, 800, 900, 1000, 1050, and 1100°C

T_{ann}, °C	ν_s(Si–O–Si), cm^{-1}	FWHM, cm^{-1}
600	805 (3)	49
700	805 (3)	51
800	811 (2)	51
900	811 (2)	56
1000	1198 (1)	16
	780 (5)	19
	796 (4)	20
1050	1198 (1)	21
	780 (5)	23
	794 (4)	21
1100	1198 (1)	27
	790 (3)	26

(comparing the samples annealed at 600–900°C), which is due to the exposure of Si–O–Si ions, associated by this type of bond, to the most intense structural rearrangement. Having in mind the influence of the temperature gradient, FWHM value confirms that the mentioned bonds are placed nearest to the surface of the samples. The narrowing of this peak (no. (1)) with heat treatment (up to 800°C, Section 3.2) indicates that the structural arrangement of the SiO_2 matrix on the sample surface enables the transition from amorphous to crystalline silica, which occurs at 1000°C. The same trend in FWHM narrowness with thermal treatment is observed for peak (2) (samples S600 and S700), confirming vanishing of silanol bonds, and further structural ordering of the SiO_2 matrix.

Noteworthy, the shift of the peaks (1) and (2) into the direction of lower wavenumbers with thermal annealing, points to the growth of nanoparticles of silica matrix, which is the main driving force for structural changes of the samples, as well for the phase transformations within the samples, during the annealing treatment of 600–800°C.

In contrast, during annealing from 800 to 900°C, there is a significant increase in the value of FWHM, as well as a shift of the peak position to higher wavenumbers. The structural changes of the silica matrix, observed during thermal treatment at 800 and 900°C, precede the phase transformation noticed at 900°C ($Fe_3O_4/\gamma\text{-}Fe_2O_3 \rightarrow \alpha\text{-}Fe_2O_3$, Section 4.1), probably by changing the size of the silica pores or by changing the silica matrix environment of these vibrations. The mentioned structural changes result in a more pronounced increase in the pore size of SiO_2, which enabled the positioning of, not only the particles that have increased in size, but also larger amounts of hematite nanoparticles (Table 1). Recall that hematite particles represent the second biggest nanoparticles in the amorphous silica matrix (only CuO nanoparticles are larger, Table 1).

Also, it could be noticed that asymmetric stretching vibrations showed significantly higher FWHM values, compared with symmetric stretching vibrations of silica, which is confirming the higher degree of structural disorder in the silica matrix surrounding these vibrations. The structural disorder is the highest in the area where the T_{grad} is the highest; i.e., the higher disorder occurs under the influence of the higher temperatures, which confirms that the structural and phase transformations begin to occur from the surface of the sample. Consequently, the asymmetric stretching vibrations are placed nearer to the surface of the silica matrix, while symmetric stretching vibrations are placed deeper in the sample.

The behavior of ν_s vibrations of the S600–S900 samples was shown to be completely different compared to ν_{as} vibrations. Exactly the same position of symmetrical vibrations for samples S600 and S700 indicates that there was no change in the bond lengths during the annealing treatment at 600 and 700°C. A very small increase in FWHM indicates a very gentle densification of the SiO_2 matrix, which is probably observed due to a more pronounced change in the crystallinity of the silica matrix around the asymmetric vibration at this temperature. This change leads to a slight structural change in the deeper, internal volume of the silica matrix.

Between 700 and 800°C, the different situation is observed: FWHM of the discussed symmetric stretching vibration retain the same value, but the bond is shifted to the higher wavenumbers (Tables 4, 5). XRD results did not allow to observe a change in the composition of the sample phases during annealing within this temperature range, but a sudden jump in the

amount of hematite phase indicate the formation of new amount of a crystallite phase at 900°C (Table 1), which is preceded by structural changes of the samples annealed between 700 and 800°C (Table 11).

Since the FWHM has retained the same value between 600 and 700°C, the crystallinity of the deeper volumes of the silica matrix does not change in the mentioned temperature range, although the shifted peak position indicate a change in the bond length. The change in crystallinity enabled a more pronounced ordering of the deeper layers of the silica matrix, which is observed in the temperature annealing interval from 800 to 900°C (Table 11). Note that FWHM of ν_s vibration is increased in this interval. Also, in this temperature range, the bond retains the same length, but the increase in the FWHM value confirms the structural ordering of the matrix.

According to Tables 10 and 11, the structural ordering of the deeper layers of the discussed samples occurs under the thermal treatment at the higher temperatures (ν_s vibrations behavior, Table 9), compared with the temperatures required for the structural ordering of the surface silica (ν_{as} bonds behavior, Table 11). The different dynamics of the structural ordering of the surface and internal silica confirms that the sample is exposed to the temperature gradient (Fig. 9).

Conclusively, the observed behavior of symmetrical stretching vibration is due to the fact that more significant structural ordering of the amorphous silica matrix occurs from 900°C (which is in accordance with XRD analysis), while the changes of the silica matrix at the surface of the sample occur regularly during the thermal treatment. Therefore, the crystallization of the silica matrix is not homogeneous throughout the sample volume, and is not an isotropic process.

On the other hand, the FTIR spectra of the crystalline SiO_2 phases also confirmed the presence of asymmetric and symmetric vibrations. Asymmetric vibration ν_{as} labeled with peak (1) in the FTIR spectrum of the sample S900, is present in the FTIR spectra of the samples annealed at 1000 and 1050°C (bonds labeled (3)), at almost the same wavenumber positions, which is an interesting result, depicting the fact that in the surrounding of this vibration, there is no more prominent change of the bond length. Another possible explanation is that all investigated samples in this temperature range contained at least two silica crystalline polymorphs, characterized by the maxima at similar wavenumber positions [88].

It should be noted that during the temperature increase from 900 to 1000°C, the FWHM of this peak is narrowed, while after annealing at 50°C increased temperature, the FWHM value of this bond increases, which results in the disappearance of the mentioned vibration at 1100°C. This observation confirms the presence of cristobalite → quartz phase transformation (Section 4.1). The (2) bond in the FTIR spectrum of the S1000 shows a shift in the direction of higher wavenumbers with increasing temperature and a slight increase in crystallinity, which is attributed to the phase transformation of quartz into tridymite.

It is difficult to comment the difference between the FTIR maxima of the cristobalite and quartz phases. The most prominent difference relies on the fact that the quartz spectrum has double peaks, which the cristobalite spectrum does not have. The characteristic quartz peaks (double peaks, Figs. 5f and 5g) are more intense, compared to the cristobalite phase (which is presented in all samples). This indicates that the quartz phase is present closer to the sample surface.

The appearance of the quartz at the surface could be a consequence of the impact of the T_{grad} onto the cristobalite (presented in the all samples containing crystalline silica, Figs. 5e–5g), placed deeper in the sample volume. The cristobalite nanoparticles, positioned closer to the surface, experience phase transformation into the quartz upon the temperature influence [125]. Dependent on the partial conversion of the cristobalite into the quartz occurred and resulted in the presence of both phases within the sample.

According to Section 4.1, the phase transformation of quartz into tridymite resulted in the tridymite phase appearance on the sample surface, instead of the quartz phase. Compared with the characteristic vibrations of cristobalite, the characteristic vibrations of trydimite are more intense (Fig. 5g), because the FTIR is a surface technique. An increase in intensity of FTIR maximum of trydimite phase could be observed even when cristobalite is present with a larger amount in the sample at the same annealed temperature (Table 1).

To summarize, the dynamics of thermal treatment of the samples initiated changes in the behavior of certain asymmetric and symmetric bonds. ν_{as} vibrations showed the pronounced change of the bond lengths with annealing treatment performed by the step of 100°C. Although a certain number of ν_s vibrations indicate no change in the bond length during the heat treatment of the sample, performed by applying a step of 100°C, a change in the length of the same vibration was observed by applying a step of 200°C, i.e., after heating the sample to a temperature which is raised by 200°C (Table 11). It is explained by the fact that ν_s bonds are placed deeper in the volume of the sample, and it is necessary to apply higher temperature step in the furnace to induce the structural rearrangement of these vibrations. This is because it is required a certain Δt, that temperature approach internal volume of the sample (compared with the temperature at the surface of the sample), and for this reason, the application of the T_{ann} that induces changes in the length of the ν_s vibrations at the surface of the sample does not induce the change of the lengths of the ν_{as} vibrations in the deeper volume of the sample. In other words, higher

steps in the increasing T_{ann} are required to change the bond lengths of the ν_s vibrations, because of the presence of the T_{grad} acting on the annealed samples.

Note that two facts from the FTIR theory support the interpretation of XRD results in the light of temperature gradient and allow confirmation of the conclusions presented in this section. First, the stretching vibrations occurred at higher wavenumbers compared to the corresponding deformation vibration (which is in accordance with the presented results, Tables 3–9), and second, more energy is required to excite the bond by asymmetric vibration (compared to symmetric vibration), i.e., asymmetric bonds are observed at higher wavenumbers compared to symmetrical vibration [125], which is in accordance with the conducted FTIR measurements in this study (Tables 10, 11). The fact that more energy is required to excite the bond to vibrate with the characteristic asymmetric vibration confirms that asymmetric vibrations of silica bonds are located at the top of the surface of the sample; i.e., more energy is generated as a consequence of the exposure of the surface part of the sample to the highest T_{grad} achieved during the thermal treatment of the sample in the furnace. Noteworthy, in the FTIR spectra of the examined samples, asymmetric vibrations are present to a higher extent compared to symmetrical vibrations (Tables 10, 11), which indicates a higher degree of structural disorder of asymmetric bonds, induced by heat treatment. With T_{grad} in mind, this also confirms that asymmetric stretching silica bonds are placed nearer to the surface of the investigated samples.

Highlights:

- Samples were prepared by the sol–gel method.
- XRD, FTIR, and CV characterization of samples were performed.
- The results of this study confirm the presence of a temperature gradient, which acts on the samples in the furnace.
- The temperature gradient affects the formation mechanism of the samples.
- The temperature gradient influences distribution of different phases with the thickness of the sample.
- The temperature gradient determines the sequence of phase transformations.

5. CONCLUSIONS

The presented study investigated the formation mechanism and phase transformations occurring in the silica matrix and in the silica matrix pores of the nanocomposite samples obtained by sol–gel method. The formation mechanism is discussed in terms of the temperature gradient, acting on the annealed sample in the furnace. The results of XRD and FTIR analyses provide a better insight in the formation mechanism of the examined samples. Accordingly, a change in the distribution of the phases in the silica matrix pores, as well as the distribution of the crystalline silica phases with the sample thickness, is proposed. The phase transformations occurring in the silica matrix and in the silica matrix pores are reflected in the cyclic voltammograms of the nanocomposite samples, recorded in 1 M KOH solution, including appearance or disappearance of characteristic oxidation/reduction peaks.

FUNDING

The research was funded by the Ministry of Education, Science and Technological Development of the Republic of Serbia.

CONFLICT OF INTEREST

The authors declare that they have no conflicts of interest.

REFERENCES

1. C. J. Brinker and G. W. Scherer, *Sol–Gel Science: The Physics and Chemistry of Sol–Gel Processing* (Academic, Boston, 1990), p. 1.
2. V. N. Nikolic, *Preparation and Characterization of Fe_2O_3-SiO_2 Nanocomposite for Biomedical Application, Mineralogy—Significance and Applications* (IntechOpen, Rijeka, 2019).
3. O. M. Lemine, K. Omri, B. Zhang, L. El Mir, M. Sajieddine, A. Alyamani, and M. Bououdina, Superlatt. Microstruct. **52**, 793 (2012).
4. Y. Sheng, J. Yang, F. Wang, L. Liu, H. Liu, C. Yan, and Z. Guo, Appl. Surf. Sci. **465**, 154 (2019).
5. N. S. Kumar, R. P. Suvarna, and K. C. B. Naidu, Mater. Chem. Phys. **223**, 241 (2019).
6. J. A. Lett, M. Sundareswari, K. Ravichandran, M. B. Latha, S. Sagadevan, and M. R. B. Johan, RSC Adv. **9**, 6228 (2019).
7. T. Fardood, S. Ramazani, A. Moradnia, F. Afshari, Z. Ganjkhanlu, and F. Yekke Zare, Chem. Methodol. **3**, 696 (2019).
8. K. Davis, R. Yarbrough, M. Froeschle, J. White, and H. Rathnayake, RSC Adv. 9, 14638 (2019).
9. R. Bao, C. Chen, J. Xia, H. Chen, and H. Li, J. Mater. Chem. C **7**, 4981 (2019).
10. K. Suzuki, S. Sato, and M. Fujita, Nat. Chem. **2**, 25 (2010).
11. F. I. H. Rhouma, F. Belkhiria, E. Bouzaiene, M. Daoudi, K. Taibi, J. Dhahri, and R. Chtourou, RSC Adv. **9**, 5206 (2019).
12. D. S. Kolchanov, V. Slabov, K. Keller, E. Sergeeva, M. V. Zhukov, A. S. Drozdov, and A. V. Vinogradov, J. Mater. Chem. C **7**, 6426 (2019).
13. A. S. Hassanien, A. A. Akl, and A. H. Saaedi, CrystEngComm **20**, 1716 (2018).

14. M. V. Berezhnaya, O. V. Almyasheva, V. O. Mittova, A. T. Nguen, and I. Y. Mittova, Russ. J. Gen. Chem. **88**, 626 (2018).
15. S. Nayak, A. Soam, J. Nanda, C. Mahender, M. Singh, D. Mohapatra, and R. Kumar, J. Mater. Sci.-Mater. Electron. **29**, 9361 (2018).
16. U. Alam, A. Khan, D. Ali, D. Bahnemann, and M. Muneer, RSC Adv. **8**, 17582 (2018).
17. W. F. Chen, S. S. Mofarah, D. A. H. Hanaor, P. Koshy, H. K. Chen, and Y. Jiang, Inorg. Chem. **57**, 7279 (2018).
18. A. H. Ashour, A. I. El-Batal, M. A. Maksoud, G. S. El-Sayyad, S. Labib, E. Abdeltwab, and M. M. El-Okr, Particuology **40**, 141 (2018).
19. K. Zheng and A. R. Boccaccini, Adv. Colloid Interface Sci. **249**, 363 (2017).
20. T. Chen, Y. Ma, Q. Guo, M. Yang, and H. Xia, J. Mater. Chem. A **5**, 3179 (2017).
21. S. T. Fardood, A. Ramazani, and S. W. Joo, J. Appl. Chem. Res. **11**, 8 (2017).
22. Y. Sheng, J. Yang, F. Wang, L. Liu, H. Liu, C. Yan, and Z. Guo, Appl. Surf. Sci. **465**, 154 (2019).
23. M. Salavati-Niasari, F. Soofivand, A. Sobhani-Nasab, M. Shakouri-Arani, M. Hamadanian, and S. Bagheri, J. Mater. Sci.: Mater. Electron. **28**, 14965 (2017).
24. B. Ritter, P. Haida, T. Krahl, G. Scholz, and E. Kemnitz, J. Mater. Chem. C **5**, 5444 (2017).
25. J. N. Hasnidawani, H. N. Azlina, H. Norita, N. N. Bonnia, S. Ratim, and E. S. Ali, Proc. Chem. **19**, 211 (2016).
26. N. N. M. Zorkipli, N. H. M. Kaus, and A. A. Mohamad, Proc. Chem. **19**, 626 (2016).
27. F. Wang, H. Li, Z. Yuan, Y. Sun, F. Chang, H. Deng, L. Xie, and H. Li, RSC Adv. **6**, 79343 (2016).
28. T. M. Wandre, P. N. Gaikwad, A. S. Tapase, K. M. Garadkar, S. A. Vanalakar, P. D. Lokhande, R. Sasikala, and P. P. Hankare, J. Mater. Sci.-Mater. Electron. **27**, 825 (2016).
29. K. M. Farhan, A. H. Ansari, M. Hameedullah, E. Ahmad, F. M. Husain, Q. Zia, and U. Baig, Sci. Rep. **6**, 27689 (2016).
30. R. M. Alwan, Q. A. Kadhim, K. M. Sahan, R. A. Ali, R. J. Mahdi, N. A. Kassim, and A. N. Jassim, J. Nanosci. Nanotechnol. **5**, 1 (2015).
31. R. Lorenzi, A. Paleari, N. V. Golubev, E. S. Ignateva, V. N. Sigaev, M. Niederberger, and A. Lauria, J. Mater. Chem. C **3**, 41 (2015).
32. N. A. Samat and R. M. Nor, Ceram. Int. **39**, S545 (2013).
33. F. Mirjalili, M. Hasmaliza, and L. C. Abdullah, Ceram. Int. **36**, 1253 (2010).
34. S. Naghibi, M. A. F. Sani, and H. R. M. Hosseini, Ceram. Int. **40**, 4193 (2014).
35. S. L. Isley and R. L. Penn, J. Phys. Chem. B **110**, 15134 (2006).
36. X. Haiyan, Z. Ai, and L. Zhang, J. Phys. Chem. C **113**, 16625 (2009).
37. C. Costa, C. Pinheiro, I. Henriques, and C. A. T. Laia, ACS Appl. Mater. Interfaces **4**, 1330 (2012).
38. L. Zhang and Y. Wu, J. Nanomater. **2013**, 1 (2013).
39. D. Prentice, M. L. Pantoya, and A. E. Gash, Energy Fuels **20**, 2370 (2006).
40. M. Grujic-Brojcin, S. Armakovic, N. Tomic, B. Abramovic, A. Golubovic, B. Stojadinovic, A. Kremenovic, B. Babic, Z. Dohcevic-Mitrovic, and M. Scepanovic, Mater. Charact. **88**, 30 (2014).
41. C. Karunakaran, P. Vinayagamoorthy, and J. Jayabharathi, Superlatt. Microstruct. **64**, 569 (2013).
42. K. L. Foo, U. Hashim, K. Muhammad, and C. H. Voon, Nanoscale Res. Lett. **9**, 429 (2014).
43. V. N. Nikolic, M. Vasic, and M. M. Milic, Ceram. Int. **44**, 21145 (2018).
44. V. N. Nikolic, M. M. Vasic, and D. Kisic, J. Solid State Chem. **275**, 187 (2019).
45. V. N. Nikolic, M. M. Milic, J. D. Zdravkovic, and V. Spasojevic, Russ. J. Phys. Chem. A **93**, 377 (2019).
46. V. N. Nikolic, M. Tadic, L. Kopanja, N. Cvjeticanin, and V. Spasojevic, Ceram. Int. **43**, 3147 (2017).
47. C. Karunakaran, V. Rajeswari, and P. Gomathisankar, Mater. Sci. Semicond. Proc. **14**, 133 (2011).
48. M. M. N. Ansari and S. Khan, Phys. B (Amsterdam, Neth.) **520**, 21 (2017).
49. I. A. Rahman and V. Padavettan, J. Nanomater. **2012**, 1 (2012).
50. T. Wang, S. H. Song, X. L. Wang, J. J. Chen, and M. L. Tan, J. Sol-Gel Sci. Technol. **85**, 356 (2018).
51. Z. Li, B. Hou, Y. Xu, D. Wu, Y. Sun, W. Hu, and F. Deng, J. Solid State Chem. **178**, 1395 (2005).
52. M. I. Zaki, G. A. Mekhemer, N. E. Fouad, T. C. Jagadale, and S. B. Ogale, Mater. Res. Bull. **45**, 1470 (2010).
53. C. Liu, B. Zou, A. J. Rondinone, and Z. J. Zhang, J. Am. Chem. Soc. **123**, 4344 (2001).
54. J. J. Beltran, C. A. Barrero, and A. Punnoose, J. Solid State Chem. **240**, 30 (2016).
55. A. Romeiro, D. Freitas, M. E. Azenha, M. Canle, and H. D. Burrows, Photochem. Photobiol. Sci. **16**, 935 (2017).
56. B. G. Trewyn, I. I. Slowing, S. Giri, H. T. Chen, and V. S. Y. Lin, Acc. Chem. Res. **40**, 846 (2007).
57. Y. Lu, Y. Yin, B. T. Mayers, and Y. Xia, Nano Lett. **2**, 183 (2002).
58. B. Manikandan, T. Endo, S. Kaneko, K. R. Murali, and R. John, J. Mater. Sci.-Mater. Electron. **29**, 9474 (2018).
59. P. K. Deheri, V. Swaminathan, S. D. Bhame, Z. Liu, and R. V. Ramanujan, Chem. Mater. **22**, 6509 (2010).
60. M. J. Pawar and A. D. Khajone, J. Chem. Pharm. Res. **4**, 1880 (2012).
61. A. E. Danks, S. R. Hall, and Z. J. M. H. Schnepp, Mater. Horiz. **3**, 91 (2016).
62. M. Alsawafta, Y. M. Golestani, T. Phonemac, S. Badilescu, V. Stancovski, and V. V. Truong, J. Electrochem. Soc. **161**, H276 (2014).
63. J. D. Mackenzie and E. P. Bescher, Acc. Chem. Res. **40**, 810 (2007).

64. S. Ramesh, J. V. Ramaclus, E. Mosquera, and B. B. Das, RSC Adv. **6**, 6336 (2016).
65. V. G. Kessler, J. Sol Gel Sci. Technol. **51**, 264 (2009).
66. Z. H. Xiao, S. H. Jin, J. H. Wang, and C. H. Liang, Hyperfine Interact. **217**, 151 (2013).
67. I. P. Prakash, N. Muralidharan, Nallamuthu, M. Venkteswarlu, and N. Satyanarayana, NSTI–Nanotech. **2**, 115 (2005).
68. N. Rajic, M. Ceh, R. Gabrovsek, and V. Kaucic, J. Am. Ceram. Soc. **85**, 1719 (2002).
69. *ICSD Inorganic Crystals Structure Database* (FIZ Karlsruhe, Eggenstein-Leopoldshafen, Germany, 2014), Vol. 2.
70. L. Lutterotti, Nucl. Instrum. Methods Phys. Res., Sect. B **268**, 334 (2010).
71. A. C. Bent, Bulletin **130**, 1 (1925).
72. D. Nicholls, *Copper, Complexes and First-Row Transition Elements* (Macmillan Education, UK, 1974), p. 281.
73. M. Meyn, K. Beneke, and C. Lagaly, Inorg. Chem. **32**, 1209 (1993).
74. R. M. Cornell and R. Giovanoli, Polyhedron **7**, 385 (1988).
75. U. Schwertmann and W. R. Fischer, Z. Anorg. Allgem. Chem. **346**, 137 (1966).
76. Y. Cudennec and A. Lecerf, J. Solid State Chem. **179**, 716 (2006).
77. R. Frison, G. Cernuto, A. Cervellino, O. Zaharko, G. M. Colonna, A. Guagliardi, and N. Masciocchi, Chem. Mater. **25**, 4820 (2013).
78. S. P. Schwaminger, D. Bauer, P. Fraga-Garcia, F. E. Wagner, and S. Berensmeier, CrystEngComm. **19**, 246 (2017).
79. L. E. Lagoeiro, J. Metamorph. Geol. **16**, 415 (1998).
80. T. S. Gendler, V. P. Shcherbakov, M. J. Dekkers, A. K. Gapeev, S. K. Gribov, and E. McClelland, Geophys. J. Int. **160**, 815 (2005).
81. K. F. McCarty, M. Monti, S. Nie, D. A. Siegel, E. Starodub, F. El Gabaly, A. H. McDaniel, A. Shavorskiy, T. Tyliszczak, H. Bluhm, N. C. Bartelt, and J. de la Figuera, J. Phys. Chem. C **118**, 19786 (2014).
82. A. U. Gehring, H. Fischer, M. Louvel, K. Kunze, and P. G. Weidler, Geophys. J. Int. **179**, 1361 (2009).
83. http://www1.lsbu.ac.uk/water/water_vibrational_spectrum.html. Accessed January 15, 2020.
84. K. Coenen, F. Gallucci, B. Mezari, E. Hensen, and M. van Sint Annaland, J. CO2 Util. **24**, 228 (2018).
85. V. Yu. Dolmatova, I. I. Kulakova, V. Myllymakic, A. Vehanenc, A. A. Bochechkad, A. N. Panovad, and B. T. T. Nguyene, J. Superhard Mater. **38**, 58 (2016).
86. L. M. Bronstein, X. Huang, J. Retrum, A. Schmucker, M. Pink, B. D. Stein, and B. Dragneam, Chem. Mater. **19**, 3624 (2007).
87. http://lisa.chem.ut.ee/IR_spectra/conservation_materials/ethanol/. Accessed December 15, 2019.
88. E. R. Lippincott, A. van Valkenburg, C. E. Weir, and E. N. Bunting, J. Res. Natl. Bur. Stand. **61**, 61 (1958).
89. H. A. Benessi and A. C. Jones, J. Phys. Chem. **63**, 179 (1959).
90. Q. Hu, H. Suzuki, H. Gao, H. Araki, W. Yang, and T. Noda, Chem. Phys. Lett. **378**, 299 (2003).
91. F. Iacona, G. Ceriola, and F. la Via, Mater. Sci. Semicond. Process. **4**, 43 (2001).
92. X. Li, Z. Cao, Z. Zhang, and H. Dang, Appl. Surf. Sci. **252**, 7856 (2006).
93. Q. Guo, D. Huang, X. Kou, W. Cao, L. Li, L. Ge, and J. Li, Ceram. Int. **43**, 192 (2017).
94. T. Gholami, M. Salavati-Niasari, M. Bazarganipour, and E. Noori, Superlatt. Microstruct. **61**, 33 (2013).
95. H. Yoshino, K. Kamiya, and H. Nasu, J. Non-Cryst. Solids **126**, 68 (1990).
96. H. Kaya, D. Ngo, S. Gin, and S. H. Kim, J. Non-Cryst. Solids **52**, 119722 (2020).
97. F. Rubio, J. Rubio, and J. L. Oteo, Spectrosc. Lett. **31**, 199 (1998).
98. K. M. Davis and M. Tomozawa, J. Non-Cryst. Solids **201**, 177 (1996).
99. R. H. Stolen and G. E. Walrafen, J. Chem. Phys. **64**, 2623 (1976).
100. J. D. Mackenzie and S. A. Rice, Phys. Today **14**, 62 (1961).
101. V. V. T. Padil and M. Cernik, Int. J. Nanomed. **8**, 889 (2013).
102. M. A. Dar, S. H. Nam, Y. S. Kim, and W. B. Kim, J. Solid State Electrochem. **14**, 1719 (2010).
103. J. Zhao, F. E. Huggins, Z. Feng, and G. P. Huffman, Clay Clay Miner. **42**, 737 (1994).
104. M. D. P. Silva, F. C. Silva, F. S. M. Sinfronio, A. R. Paschoal, E. N. Silva, and C. W. A. Paschoal, J. Alloys Compd. **584**, 573 (2014).
105. W. P. Gates, J. T. Kloprogge, J. Madejová, and F. Bergaya, *Infrared and Raman Spectroscopies of Clay Minerals* (Elsevier, Amsterdam, 2017), p. 1.
106. R. S. Pandurangi, M. S. Seehra, B. L. Razaboni, and P. Bolsaitist, Environ. Health Perspect. **86**, 327 (1990).
107. A. P. Mirgorodskii, A. N. Lazarev, and I. P. Makarenko, Opt. Spectrosc. **29**, 282 (1970).
108. B. P. Jelle, T.-N. Nilsen, P. J. Hovde, and A. Gustavsen, J. Build. Phys. **36**, 99 (2012).
109. V. N. Nikolic, Magn. Nanomater. Electrocatal., Magnetochem.: Mater. Appl. **66**, 34 (2020).
110. M. Catauro, F. Barrino, G. Dal Poggetto, G. Crescente, S. Piccolella, and S. Pacifico, Materials **13**, 394 (2020).
111. A. Jitianu, M. Crisan, A. Meghea, I. Rau, and M. Zaharescu, J. Mater. Chem. **12**, 1401 (2002).
112. G. Anbalagan, A. R. Prabakaran, and S. Gunasekaran, J. Appl. Spectrosc. **77**, 95 (2010).
113. P. C. Schlecht and P. F. O'Connor, *Third Supplement to NIOSH Manual of Analytical Methods (NMAM)*, 4th ed. (Natl. Inst. Occup. Safety and Health, 2003).
114. J. Hlavay, K. Jonas, S. Elek, and J. Inczedy, Clay. Clay Miner. **26**, 139 (1978).

115. E. Nemecz and K. Rethy, Rep. Veszp. Univ. Chem. Eng. **5**, 287 (1961).
116. L. B. Capeletti and J. H. Zimnoch, *Fourier Transform Infrared and Raman Characterization of Silica-Based Materials, Applications of Molecular Spectroscopy to Current Research in the Chemical and Biological Sciences* (IntechOpen, Rijeka, Croatia, 2016).
117. M. Cekerevac, M. Simicic, Lj. N. Bujanovic, and N. Popovic, Corros. Sci. **64**, 204 (2012).
118. M. J. Song, S. W. Hwang, and D. Whang, Talanta **80**, 1648 (2010).
119. J. Ping, S. Ru, K. Fan, J. Wu, and Y. Ying, Microchim. Acta **171**, 117 (2010).
120. T. M. Nahir and E. F. Bowden, J. Electroanal. Chem. **410**, 9 (1996).
121. H. H. Uhlig and J. R. Gilman, Corrosion **20**, 289t (1964).
122. S. D. Giri and A. Sarkar, J. Electrochem. Soc. **163**, H252 (2016).
123. J. Coates, *Interpretation of Infrared Spectra, A Practical Approach, Encyclopedia of Analytical Chemistry: Applications, Theory and Instrumentation* (Wiley, New York, 2007).
124. R. Bruckner, J. Non-Cryst. Solids **5**, 123 (1970).
125. A. C. D. Chaklader and A. L. Roberts, J. Am. Ceram. Soc. **44**, 35 (1961).